The Astrophysical Journal, 756:28 (16pp), 2012 September 1 doi:10.1088/0004-637X/756/1/28

SPITZER-IRAC IDENTIFICATION OF *HERSCHEL*-ATLAS SPIRE SOURCES

Sam Kim[1], Julie L. Wardlow[1], Asantha Cooray[1], S. Fleuren[2], W. Sutherland[2], A. A. Khostovan[1], R. Auld[3], M. Baes[4], R. S. Bussmann[5,19], S. Buttiglione[6], A. Cava[7], D. Clements[8], A. Dariush[8], G. De Zotti[6,9], L. Dunne[10], S. Dye[11], S. Eales[3], J. Fritz[4], R. Hopwood[8], E. Ibar[12], R. Ivison[12], M. Jarvis[13,14], S. Maddox[10], M. J. Michałowski[15], E. Pascale[3], M. Pohlen[3], E. Rigby[10], D. Scott[16], D. J. B. Smith[13], P. Temi[17], and P. van der Werf[18]
[1] Department of Physics and Astronomy, University of California, Irvine, CA 92697, USA
[2] School of Physics and Astronomy, Queen Mary University of London, Mile End Road, London E1 4NS, UK
[3] School of Physics and Astronomy, Cardiff University, Cardiff CF24 3AA, UK
[4] Sterrenkundig Observatorium, Universiteit Gent, Krijgslaan 281 S9, B-9000 Gent, Belgium
[5] Harvard-Smithsonian Center for Astrophysics, 160 Concord Avenue, Cambridge, MA 02138, USA
[6] INAF-Osservatorio Astronomico di Padova, Vicolo Osservatorio 5, I-35122 Padova, Italy
[7] Departamento de Astrofísica, Facultad de CC. Físicas, Universidad Complutense de Madrid, E-28040 Madrid, Spain
[8] Physics Department, Imperial College London, South Kensington Campus, London SW7 2AZ, UK
[9] SISSA, Via Bonomea 265, I-34136 Trieste, Italy
[10] Department of Physics and Astronomy, University of Canterbury, Private Bag 4800, Christchurch, 8041, New Zealand
[11] School of Physics and Astronomy, University of Nottingham, University Park, Nottingham NG7 2RD, UK
[12] UK Astronomy Technology Centre, Royal Observatory, Blackford Hill, Edinburgh EH9 3HJ, UK
[13] Centre for Astrophysics Research, Science & Technology Research Institute, University of Hertfordshire, Hatfield, Herts AL10 9AB, UK
[14] Physics Department, University of the Western Cape, Cape Town 7535, South Africa
[15] Scottish Universities Physics Alliance, Institute for Astronomy, University of Edinburgh, Royal Observatory, Edinburgh EH9 3HJ, UK
[16] Department of Physics and Astronomy, University of British Columbia, 6224 Agricultural Road, Vancouver, BC V6T1Z1, Canada
[17] Astrophysics Branch, NASA/Ames Research Center, MS 245-6, Moffett Field, CA 94035, USA
[18] Leiden Observatory, Leiden University, P.O. Box 9513, 2300 RA Leiden, The Netherlands
Received 2011 December 15; accepted 2012 June 29; published 2012 August 10

ABSTRACT

We use *Spitzer*-IRAC data to identify near-infrared counterparts to submillimeter galaxies detected with *Herschel*-SPIRE at 250 μm in the *Herschel* Astrophysical Terahertz Large Area Survey. Using a likelihood ratio analysis we identify 146 reliable IRAC counterparts to 123 SPIRE sources out of the 159 in the survey area. We find that, compared to the field population, the SPIRE counterparts occupy a distinct region of the 3.6 and 4.5 μm color–magnitude space, and we use this property to identify 23 further counterparts to 13 SPIRE sources. The IRAC identification rate of 86% is significantly higher than those that have been demonstrated with wide-field ground-based optical and near-IR imaging of *Herschel* fields. We estimate a false identification rate of 3.6%, corresponding to 4–5 sources. Among the 73 counterparts that are undetected in Sloan Digital Sky Survey, 57 have both 3.6 and 4.5 μm coverage. Of these, 43 have $[3.6]-[4.5]>0$, indicating that they are likely to be at $z\gtrsim 1.4$. Thus, ∼40% of identified SPIRE galaxies are likely to be high-redshift ($z\gtrsim 1.4$) sources. We discuss the statistical properties of the IRAC-identified SPIRE galaxy sample including far-IR luminosities, dust temperatures, star formation rates, and stellar masses. The majority of our detected galaxies have 10^{10}–10^{11} $L_{\odot}$ total IR luminosities and are not intense starbursting galaxies as those found at $z\sim 2$, but they have a factor of 2–3 above average specific star formation rates compared to near-IR selected galaxy samples.

Key words: galaxies: high-redshift – galaxies: starburst – infrared: galaxies

Online-only material: color figures

1. INTRODUCTION

The extragalactic background at far-infrared (IR) and submillimeter (sub-mm) wavelengths is well constrained from total intensity measurements (Puget et al. 1996; Fixsen et al. 1998; Dwek et al. 1998). However, the properties of the discrete galaxies that make up this background are still largely unknown. These sub-mm galaxies are expected to capture the dusty star formation out to redshifts of 4 and beyond and are now understood to be an integral component of galaxy formation and evolution (Hughes et al. 1998; Eales et al. 1999; Blain et al. 2002; Chapman et al. 2003; Austermann et al. 2010).

A challenge for studies of sub-mm galaxies is that wide-field surveys at these wavelengths have poor spatial resolution, caused by the limited apertures of single dish sub-mm survey telescopes (Smail et al. 1997; Scott et al. 2002; Coppin et al. 2006). Typical resolutions are of the order of tens of arcseconds, making the identification of multiwavelength counterparts challenging, particularly in the optical where sub-mm galaxies are usually faint due to high dust extinction. Furthermore, the surface density of faint optical galaxies is such that several potential counterparts may be situated within the positional error of each sub-mm source. However, the identification of counterparts to sub-mm galaxies is critical for both photometric and spectroscopic studies, which yield redshifts, spectral energy distributions (SEDs), and morphological information. The measurements of these quantities for statistically significant samples of sub-mm galaxies are required to compare their properties with theoretical predictions, and to fully understand the role of the sub-mm bright phase in galaxy evolution.

The most reliable way to pinpoint the positions of sub-mm galaxies is through high-resolution sub-mm interferometry, which directly traces the dust emission at wavelengths comparable to the original selection function (e.g., Downes et al. 1999;

[19] Submillimeter Array Fellow.

Gear et al. 2000; Iono et al. 2006; Younger et al. 2007). The sensitivity of early generations of sub-mm interferometric instrumentation limited analyses to samples of no more than a few sources (e.g., Downes et al. 1999; Gear et al. 2000; Iono et al. 2006; Younger et al. 2007, 2008, 2009; Ivison et al. 2008; Cowie et al. 2009; Aravena et al. 2010a; Hatsukade et al. 2010; Tamura et al. 2010; Chen et al. 2011), and although rapid progress is being made (e.g., Smolčić et al. 2012a, 2012b) such observations are still unfeasible for large surveys of sources. In addition, extended sources (e.g., Matsuda et al. 2007), or sources that are a blend of multiple components (e.g., Wang et al. 2011; Smolčić et al. 2012a), can be difficult to detect.

An alternative technique to identify sub-mm galaxies is to take advantage of the far-IR–radio correlation (e.g., Condon et al. 1998; Garrett 2002) and the relatively low surface density of radio sources by searching for counterparts in deep interferometric radio data (e.g., Ivison et al. 1998, 2002; Borys et al. 2004; Dye et al. 2009; Dunlop et al. 2010; Biggs et al. 2011). Similarly, the dusty, active sub-mm galaxies are typically bright at mid-IR wavelengths, a property that has also been utilized to identify counterparts (e.g., Ivison et al. 2004; Pope et al. 2006; Dye et al. 2008, 2009; Clements et al. 2008; Dunlop et al. 2010; Biggs et al. 2011). Deep radio and mid-IR (typically *Spitzer* MIPS 24 μm but also *Spitzer*-IRAC 3.6 μm; Biggs et al. 2011) searches typically identify counterparts to 60%–80% of sub-mm galaxies, and nearest-neighbor positional matching is then used to investigate the properties of these sources at other wavelengths. The remaining 20%–40% of sources are thought to be at high redshifts ($z \gtrsim 3$) or be dominated by cold dust ($T_D \lesssim 25$ K at $z \sim 2$; Chapman et al. 2005).

The *Herschel* Astrophysical Terahertz Large Area Survey (H-ATLAS; Eales et al. 2010) is the largest open-time key project being undertaken by the *Herschel Space Observatory* (Pilbratt et al. 2010).[20] The total planned survey area is 550 deg^2 within which it is expected to detect >300,000 bright sub-mm galaxies. During the Science Demonstration Phase (SDP), H-ATLAS observed 14.4 deg^2 in the Galaxy And Mass Assembly (GAMA; Driver et al. 2011) 9 hr field, to 5σ depths of 35–132 mJy in five bands from 100 to 500 μm, using PACS (100 and 160 μm; Poglitsch et al. 2010) and SPIRE (250, 350, and 500 μm; Griffin et al. 2010) in parallel mode. The lack of deep radio and 24 μm data across the field restricts counterpart identification to optical (e.g., Sloan Digital Sky Survey (SDSS); York et al. 2000) or near-IR data (e.g., VISTA Kilo-Degree Infrared Galaxy Survey (VIKING), W. Sutherland et al., in preparation; UKIRT Infrared Deep Sky Survey (UKIDSS), Lawrence et al. 2007).

Smith et al. (2011) identified SDSS and GAMA galaxies as the counterparts to 37% of the SPIRE sources in the H-ATLAS SDP field. In the wider area of the whole GAMA 9 hr field, Fleuren et al. (2012) increased the fraction of SPIRE sources with reliable identifications to 51% by using K_s-band imaging from the VIKING survey. In the GAMA 15 hr field, 50% of the SPIRE sources have reliable counterparts identified in *Wide-Field Infrared Survey Explorer* (*WISE*) data at 3.4 μm (Bond et al. 2012).

In this paper, we cross-identify H-ATLAS SPIRE sources with *Spitzer* Infrared Array Camera (IRAC; Fazio et al. 2004b) galaxies, which are selected from 3.6 and 4.5 μm observations of 0.4 deg^2 of the H-ATLAS SDP field. The IRAC data are advantageous for counterpart identification because of their mid-IR wavelengths and depth (~3 mag deeper than *WISE*). Thus, counterpart identification is less biased toward galaxies with relatively low redshifts or dust obscurations than the existing analyses.

The paper is organized as follows: the data analysis and sample selection are presented in Section 2. In Section 3 we describe the counterpart identification method, and in Section 4 we discuss our results, including the identification rate and the colors and properties of SPIRE counterparts. Our conclusions are presented in Section 5. The identified counterparts, including magnitudes and fluxes, are presented in Table 2. We use J2000 coordinates and ΛCDM cosmology with $\Omega_m = 0.27$, $\Omega_\Lambda = 0.73$, and $H_0 = 70\,\mathrm{km\,s^{-1}\,Mpc^{-1}}$ throughout. All photometry is on the AB magnitude system where 1 μJy = 23.9 mag; IRAC 3.6 and 4.5 μm AB magnitudes are designated [3.6] and [4.5], respectively.

2. SAMPLE SELECTION AND DATA ANALYSIS

The H-ATLAS fields were chosen to minimize contamination from Galactic cirrus and to maximize the overlap with existing and planned wide-area imaging and spectroscopic surveys. The SDP field, which we study here, spans ~14 deg^2 in the GAMA 9 hr field and has existing SDSS, VIKING, and UKIDSS data. It is observed with PACS at 100 and 160 μm and SPIRE at 250, 350, and 500 μm. The H-ATLAS PACS and SPIRE map-making processes are described in Ibar et al. (2010) and Pascale et al. (2011), respectively, and details of the source extraction procedures are given in Rigby et al. (2011). A public catalog of SDP sources is available from the H-ATLAS Web site.[21] The data reach 5σ point-source depths of 132, 126, 32, 36, and 45 mJy, with beam sizes of 8.7, 13.1, 18.1, 25.2, and 36.″9 (FWHM) at 100, 160, 250, 350, and 500 μm, respectively. Although PACS 100 and 160 μm data have significantly higher angular resolution than SPIRE data, we do not use PACS data for counterpart identification because only 5 of the 159 SPIRE sources studied here are detected by PACS. In all five cases, the position of the identified IRAC counterpart (Table 2) is consistent with the PACS emission. Furthermore, the counterparts to all of these five sources are low-redshift late-type galaxies, which is consistent with expectations for galaxies that are detectable with PACS.

Spitzer-IRAC 3.6 and 4.5 μm staring mode observations of 0.4 deg^2, in three regions of the H-ATLAS SDP field, were carried out during the warm mission (*Spitzer* program 548; PI: A. Cooray). Two of the areas targeted contain bright SPIRE SDP sources that are now known to be gravitationally lensed (ID81 and ID130; Negrello et al. 2010; Hopwood et al. 2011) and the third area was chosen as a test field. In staring mode, simultaneous observations at 3.6 and 4.5 μm are offset from each other by 6.′8. Due to the offset, 0.22 deg^2 of the targeted area has imaging data at both 3.6 and 4.5 μm, and the remaining 0.18 deg^2 is split between 3.6 and 4.5 μm coverage. There are 159 SPIRE sources in the total IRAC footprint. Of these, 101 are observed at both 3.6 and 4.5 μm, and 30 (28) have only 3.6 μm (4.5 μm) data. The total exposure time is 1080 s pixel^{-1} in each filter. Data reduction and mosaicking is performed on the corrected basic calibrated data with MOPEX (MOsaicker and Point source EXtractor; Makovoz & Marleau 2005). The final mosaicked images have 0.″6 × 0.″6 pixels and the FWHM of the

[20] *Herschel* is an ESA space observatory with science instruments provided by European-led Principal Investigator consortia and with important participation from NASA.

[21] http://www.h-atlas.org

IRAC point-spread function at 3.6 and 4.5 μm is 1.″66 and 1.″72, respectively.

Our source detection and extraction procedure is designed to simultaneously select sources at 3.6 and 4.5 μm, and provide equivalent photometry in both bands. The source detection is performed on a mean combined 3.6 and 4.5 μm image. The 3.6 and 4.5 μm image combination is carried out with Montage,[22] which models background flux by co-adding and re-projecting background corrected images into a mosaic. Source detection is performed with SExtractor (Bertin & Arnouts 1996) and detected sources are required to comprise at least three contiguous pixels with fluxes at least 1.5σ above the local background. There are 27,170 unique 3.6 and 4.5 μm sources that meet this requirement and that are detected at $\geqslant 5\sigma$. Photometry is measured in 3.″8 diameter apertures with the apphot task in iraf. The advantage of apphot is that the photometry is measured in fixed apertures at specified source positions. The measured aperture photometry is corrected to "total" fluxes, assuming point-source profiles, and using the calibration derived by the SWIRE team for IRAC data with multiplicative correction factors of 1.36 and 1.40 at 3.6 and 4.5 μm, respectively (Surace et al. 2005).

The completeness of the IRAC catalog is established by inserting artificial galaxies with a maximum half-light radius of 1.″5 in the IRAC images. Our source extraction and photometric procedure is repeated and a source is considered to be recovered if the extracted position and magnitude are within 1.″5 and 5σ, respectively, of the input values. The 50% completeness limits are 22.5 mag (3.63 μJy) and 22.2 mag (4.79 μJy) at 3.6 and 4.5 μm, respectively.

The far-IR emission detected by SPIRE traces emission from cold dust. Therefore, point sources in blank-field surveys, such as H-ATLAS, are primarily expected to be external galaxies and not stars in the Milky Way. Indeed, of the ~6600 SPIRE sources in ~14 deg^2 in the H-ATLAS SDP field only 78 are Galactic stars, and 2 are candidate debris disks (Thompson et al. 2010). Since stars dominate the IRAC catalog at the brightest fluxes and have magnitude distributions that are different to galaxies, it is necessary to remove them prior to counterpart identification (e.g., Smith et al. 2011). Unfortunately the angular resolution of IRAC (FWHM ~ 1.″7) is insufficient to morphologically distinguish between stars and high-redshift galaxies. Furthermore, while stars can be identified in [3.6] − [4.5] color–magnitude space (e.g., Eisenhardt et al. 2004) we are limited to just single IRAC band data for ~45% of the total IRAC catalog.

Therefore, instead of using IRAC data alone to reliably identify stars, we make use of the stellar classification in SDSS. For this we match the IRAC catalog to SDSS DR7 (Abazajian et al. 2009) using positional information. ~40% of IRAC sources are matched with SDSS catalog within search radius 1.″5. Out of the total 27,170 IRAC sources, there are 4239 (16%) sources that are classified as stars by SDSS. Once these are removed, the final IRAC catalog has 22,931 galaxies. This catalog is used for the SPIRE source identification and subsequent analysis. We note that Fazio et al. (2004a) showed that faint stars are an only minor contribution to the IRAC population, with $<10^3$ mag^{-1} deg^{-2} for magnitudes fainter than 16 mag at both 3.6 and 4.5 μm. Therefore, stars that are too faint to be detected as such by SDSS are not expected to affect our statistical analysis.

[22] http://montage.ipac.caltech.edu

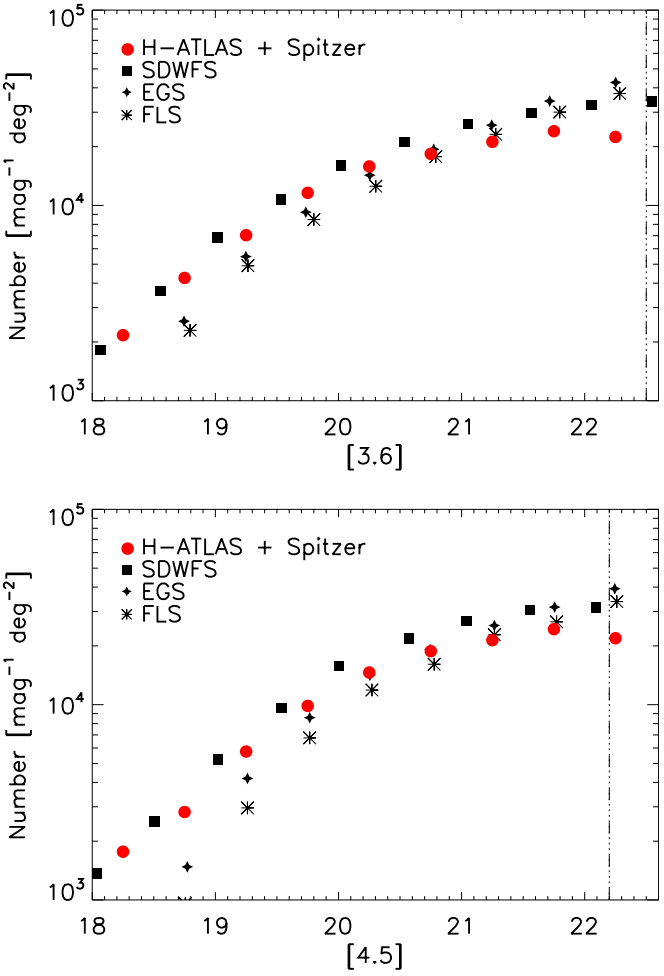

Figure 1. Galaxy number counts from H-ATLAS/*Spitzer* area compared with previous IRAC deep and wide fields: SDWFS (Ashby et al. 2009), First Look Survey (FLS; Fazio et al. 2004a), and EGS (Barmby et al. 2008). H-ATLAS galaxy counts are more consistent with SDWFS. The 50% IRAC completeness limits of our imaging at 22.5 and 22.2 mag at 3.6 and 4.5 μm, respectively, are indicated by vertical dash-dot-dot lines. 5σ detection limit of SDWFS with 3″ aperture is 22.8 and 22.3 mag at 3.6 and 4.5 μm, respectively.

(A color version of this figure is available in the online journal.)

In addition, SDSS QSO population statistics (Schneider et al. 2007) indicate that only 2–3 QSOs are expected in the IRAC area (<1 in the counterpart search area around SPIRE centroids), and therefore the effect of QSOs on our statistics is also expected to be negligible. We conclude that the counterpart identification statistics are unlikely to be affected by unresolved source contamination in our input catalog.

In Figure 1, we compare the IRAC galaxy counts in H-ATLAS/*Spitzer* area with some of the previous IRAC deep and wide fields. H-ATLAS galaxy counts are more consistent with SDWFS (Ashby et al. 2009), although the variations between fields are likely to be due to cosmic variance.

3. *SPITZER*-IRAC IDENTIFICATION OF SPIRE SOURCES

The size of the SPIRE beam is 18.″1 (FWHM) at 250 μm, and 25.″2 and 36.″9 at 350 and 500 μm, respectively. The spatial density of IRAC-bright galaxies is high enough that multiple sources may lie within the SPIRE beam. Typically, this will include the true SPIRE counterpart and unassociated foreground and background galaxies. However, the surface density of 250 μm bright sources is sufficient that a single SPIRE source

may be composed of emission from multiple galaxies. Therefore, choosing the nearest object as the counterpart of a given SPIRE source can be misleading. Instead, we perform a likelihood ratio (LR) analysis (Section 3.1; Sutherland & Saunders 1992; Ciliegi et al. 2003; Brusa et al. 2007; Smith et al. 2011; Fleuren et al. 2012), which uses positional information and the magnitude distribution of counterparts and background sources, to identify SPIRE sources in the IRAC catalog. Furthermore, the LR analysis shows that galaxies associated with SPIRE sources occupy a distinct region of IRAC color–flux space (Figure 4), which we use in Section 3.4 to identify additional counterparts.

We note that other statistical matching techniques have been used in astronomical implementations. For example, the corrected Poissonian probability (p-statistic; Downes et al. 1986) uses the surface density to calculate the probability of a source with the observed magnitude being detected within the radius investigated (e.g., Ivison et al. 2002, 2007; Pope et al. 2006; Chapin et al. 2009). However, this technique is most appropriate for catalogs in which the surface density is low (e.g., radio data) and favors counterparts that are brighter than the background population. Our IRAC data do not have low-surface density, and we do not wish to assume that the *Herschel* counterparts are typically the brightest IRAC sources. Bayesian techniques (e.g., Budavári & Szalay 2008), which use a priori knowledge of the counterpart population to guide the identification process, could also be employed (e.g., Brand et al. 2006; Gorjian et al. 2008). However, we do not wish to bias our results by assuming a priori knowledge of the SPIRE population at IRAC wavelengths. The LR analysis is advantageous because it computes the intrinsic IRAC magnitude distribution of the SPIRE sources from the data provided (see, e.g., Fleuren et al. 2012).

3.1. The Likelihood Ratio Method

The LR, L, is the ratio of the probability that the IRAC source is the correct SPIRE counterpart with the equivalent probability for an unassociated background source. Following Sutherland & Saunders (1992), L is calculated as

$$L = \frac{q(m)f(r)}{n(m)}, \quad (1)$$

where $q(m)$ and $n(m)$ are the normalized magnitude distributions of counterparts and background sources, respectively. The radial probability distribution of the separation between the SPIRE 250 μm and IRAC positions is denoted by $f(r)$.

We estimate $n(m)$, the normalized magnitude distribution of background sources, by averaging the source counts in areas of circle within 7.″2 radius of 100 different realizations of 159 random positions. The radius is three times the positional uncertainty of the SPIRE catalog. We use $\sigma_{\rm pos} = 2.''4 \pm 0.''9$ (Smith et al. 2011) calculated in the H-ATLAS SDP field from the positional offsets between SDSS DR7 galaxies and 6621 SPIRE sources. The center of each random circle is required to be at least 15″ away from the nearest SPIRE centroid to minimize possible contamination of real association. The quantity $q(m)$, the normalized magnitude distribution of true IRAC counterparts to SPIRE sources, cannot be directly derived. We empirically estimate $q(m)$ by first subtracting the magnitude distribution of background galaxies from the magnitude distribution of all IRAC sources within search radius.

This results in an estimate of the magnitude distribution of sources that are in excess of the background, $N_{\rm excess}(m)$, and assumed to be the true counterparts to SPIRE sources. Then, $q(m)$ is calculated via

$$q(m) = \frac{N_{\rm excess}(m)}{\sum_m N_{\rm excess}(m)} \times Q_0, \quad (2)$$

where Q_0 is the fraction of true counterparts above the IRAC detection limit. The [3.6] and [4.5] distributions of $n(m)$ and $N_{\rm excess}(m)$ are shown in Figure 2.

The radial probability distribution, $f(r)$, is given by

$$f(r) = \frac{1}{2\pi\sigma_{\rm pos}^2} \exp\left(\frac{-r^2}{2\sigma_{\rm pos}^2}\right), \quad (3)$$

where r is the separation between the SPIRE 250 μm and IRAC centroids, and $\sigma_{\rm pos}$ is the positional uncertainty of the SPIRE

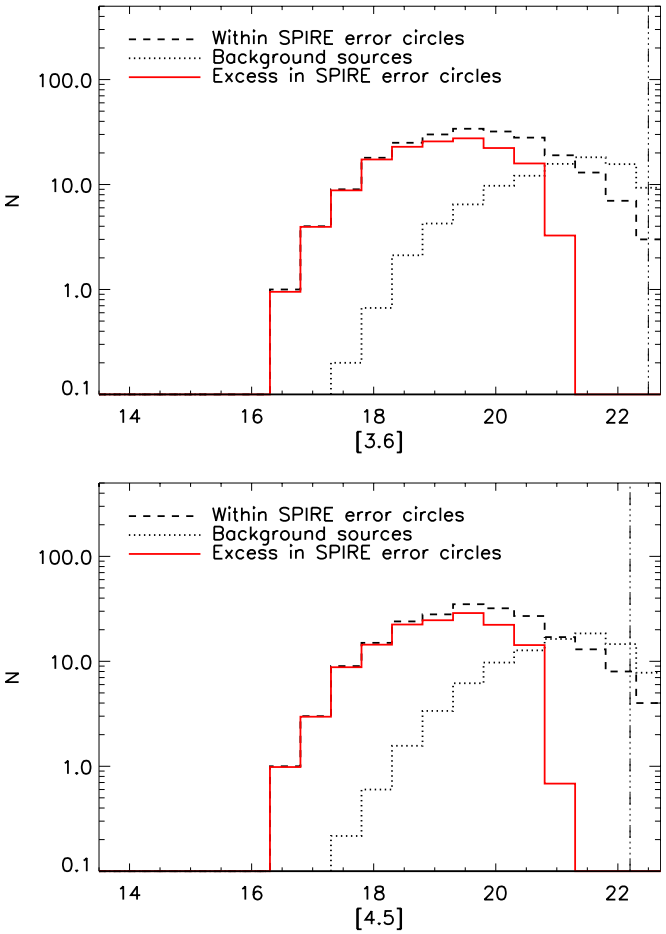

Figure 2. Magnitude distribution of IRAC galaxies at 3.6 (top) and 4.5 μm (bottom) within the 7.″2 counterpart search radius around SPIRE sources. We calculate the distribution of background galaxies and subtract these to reveal an excess around SPIRE sources which peaks at 19.0 mag at both 3.6 and 4.5 μm. These are the magnitude distributions of detected IRAC galaxies that are associated with SPIRE sources. The magnitude distribution of background sources is obtained by averaging the counts within 7.″2 of 100 different realizations of 159 random positions that are each >15″ from the nearest SPIRE centroid. To reduce the Poisson fluctuations associated with the small sample of 159 SPIRE centroids, the magnitude distribution of IRAC counts within SPIRE error circles is averaged over two bins. The 50% *Spitzer*-IRAC completeness limits of 22.5 and 22.2 mag at 3.6 and 4.5 μm, respectively, are indicated by vertical dash-dot-dot lines. All of the excess galaxies that are associated with SPIRE sources are brighter than these detection limits indicating that the IRAC data are sufficiently deep to detect counterparts to all typical SPIRE sources.

(A color version of this figure is available in the online journal.)

catalog. The median 250 μm signal-to-noise ratio (S/N) of the SPIRE sources in our sample is 6.33 and only 43 (27%) have S/N $>$ 8. Therefore, we ignore the improvement in $\sigma_{\rm pos}$ for sources with high S/N (Smith et al. 2011).

Each H-ATLAS source may have several potential counterparts. Therefore, we calculate the reliability, R_j, of each IRAC galaxy, j, in SPIRE counterpart search radius. R_j is the probability that the galaxy, j, is the correct IRAC counterpart to the SPIRE source. Following Sutherland & Saunders (1992),

$$R_j = \frac{L_j}{\sum_i L_i + (1 - Q_0)}, \quad (4)$$

where i represents each IRAC source in the search radius.

To accept a potential counterpart as reliable we require that $R_j \geqslant 0.8$, i.e., there is <20% chance of a false association. This criterion was used by Smith et al. (2011) for the counterpart search with SDSS data and our results on the identification rate with IRAC data can be directly compared to their results based on optical imaging. We note that the choice of the exact limiting value of R does not strongly affect our conclusions. Of the 123 SPIRE sources with $R \geqslant 0.8$ counterparts (Section 3.3), 107 (87%) have $R \geqslant 0.9$, and 101 (82%) have $R \geqslant 0.95$.

For a catalog in which identified sources are required to have $R \geqslant 0.8$ the overall false detection rate is

$$N(\text{false}) = \sum_{R_j \geqslant 0.8} (1 - R_j). \quad (5)$$

3.2. Q_0 Calculation

In order to apply the LR method to the SPIRE and IRAC catalogs we must first compute Q_0. Smith et al. (2011) calculated Q_0 from the total number of SDSS galaxies in the error circles of SPIRE sources. However, this method requires some a priori chosen radius and is only valid if each SPIRE source is associated with only one SDSS galaxy. Instead, we make use of an alternative method, derived by Fleuren et al. (2012), which is radius independent and unaffected by the clustering of IRAC sources. Clustering can be a significant complication because SPIRE sources are expected to reside in overdense regions similar to environments of sub-mm galaxies (e.g., Aravena et al. 2010b; Hickox et al. 2012).

For the purposes of this discussion, we define a SPIRE error circle without a true IRAC counterpart as a "*blank*." Directly observed blanks arise due to counterparts below the IRAC detection limit or beyond the search radius, r. However, the total number of blanks must also be statistically corrected for contamination by unassociated foreground or background galaxies. Thus, the true number of blanks ($\bar{S}_t$) is equal to the number of observed SPIRE blanks ($\bar{S}(r)$) and the number of SPIRE sources that are falsely matched with random background galaxies. We define $R_o(r)$ as the number of random positions that contain an IRAC galaxy while $\bar{R}(r) = N - R_o(r)$ is the number of random blanks. Then,

$$\bar{S}_t = \bar{S}(r) + \left[\bar{S}_t \times \frac{R_o(r)}{N}\right], \quad (6)$$

with $R_o(r)$ and $\bar{R}(r)$ calculated from 100 random realizations of $N = 159$ error circles, which are all located at least 15″ away from SPIRE centroids.

Q_0 is defined as the fraction of true counterparts above the IRAC detection limit. Thus, for an infinite search radius, the rate of true blanks, $\bar{S}_t/N$, is simply equal to $1 - Q_0$. Fleuren et al. (2012) demonstrate that Equation (6) can be rearranged to show that $\bar{S}_t/N = \bar{S}(r)/\bar{R}(r)$, and thus $1 - Q_0 = \bar{S}(r)/\bar{R}(r)$.

However, there is also the possibility that the true counterpart is outside of the examined area and this must be accounted for in the Q_0 estimate. The probability that the real SPIRE source is outside the search radius can be derived analytically from the normalized SPIRE source distribution, $f(r)$ (Equation (3)). This probability, $F(r)$, is

$$F(r) = \int_0^r P(r')\,dr' = 1 - e^{-\frac{r^2}{2\sigma^2}}, \quad (7)$$

where $P(r) = 2\pi r f(r)$ (Fleuren et al. 2012). Assuming that the probability of a SPIRE source being a true blank ($1 - Q_0$) and the probability that the detected counterpart is outside of the search radius ($1 - F(r)$) are independent, it can be shown that the total probability that there is no counterpart is (see Fleuren et al. 2012)

$$\frac{\bar{S}_t}{N} = 1 - Q_0 F(r). \quad (8)$$

However, we have already shown that $\bar{S}_t/N = \bar{S}(r)/\bar{R}(r)$. Thus, using the observables $\bar{S}(r)$ and $\bar{R}(r)$ one can calculate Q_0 via $1 - Q_0 F(r) = \bar{S}(r)/\bar{R}(r)$. Figure 3 shows $\bar{S}(r)/\bar{R}(r)$, $\bar{R}(r)/N$, and $\bar{S}(r)/N$, observed for search radii of one to 10″. We calculate the constant, Q_0, by fitting $1 - Q_0 F(R)$ to $\bar{S}(r)/\bar{R}(r)$. χ^2 minimization yields $Q_0 = 0.93 \pm 0.09$, 0.92 ± 0.08 at 3.6 and 4.5 μm, respectively.

3.3. LR Counterparts

We apply the LR technique outlined in Sections 3.1 and 3.2 at 3.6 and 4.5 μm, to identify IRAC counterparts to 123 of 159 H-ATLAS SPIRE sources (Tables 1 and 2). $q(m)$ and $n(m)$ are calculated in a radius of $3\sigma_{\rm pos} = 7\farcs2$ (although Q_0 is radius independent; Section 3.2) and only IRAC galaxies within 7.″2 of SPIRE sources are considered to be potential counterparts. This limit includes 99.7% of true counterparts, while minimizing the potential contamination from unassociated sources. The analysis is performed separately at 3.6 and 4.5 μm and any IRAC galaxy with $R \geqslant 0.8$ at either wavelength is considered to be a SPIRE counterpart. In addition, where both 3.6 and 4.5 μm data are available we combine the probabilities (R) from each wavelength, and include five counterparts that have a combined probability of being considered to be reliable identifications $\geqslant$0.8, but have $R < 0.8$ at 3.6 and 4.5 μm individually. All 123 counterparts are presented in Table 2, including 81 galaxies with both 3.6 and 4.5 μm photometry. The false identification rate is 1.9% or approximately two sources (Equation (5)); in the case of counterparts that are identified at both 3.6 and 4.5 μm, we use the highest of the two R_j in this calculation.

The identification rate of 77% is significantly higher than that from optical (37% in SDSS; Smith et al. 2011) or near-IR analyses (51% in VIKING; Fleuren et al. 2012) of H-ATLAS sources. This difference is likely to be primarily driven by the wavelengths of the study, which are less sensitive to K-correction and dust absorption than optical data.

The counterpart identification rate is also significantly higher than the 50% obtained with *WISE* 3.4 μm data (Bond et al. 2012); this is true even if we only consider the 3.6 μm data, where 97 of the 129 SPIRE sources with 3.6 μm coverage (75%) are identified. *WISE* is shallower than our IRAC observations—19.7 mag at 3.4 μm compared to 22.5 mag at

Table 1
Summary of IRAC Counterparts to SPIRE Sources

Method	$N_{\rm SPIRE}$[a]	$N_{\rm ID}$[b]	ID Rate[c]	$N_{\rm IRAC}$[d]	$N_{\rm multiple}$[e]	Contamination Rate
LR	159	123	77%	123	0	1.9%
Color–Magnitude	19	13	68%	23	7	12.6%
Total	159	136	86%	146	7	3.6%

Notes.
[a] Number of SPIRE sources considered.
[b] Number of SPIRE sources with at least one counterpart.
[c] Fraction of SPIRE sources with at least one identified counterpart.
[d] Number of IRAC counterparts identified.
[e] Number of SPIRE sources with multiple IRAC counterparts.

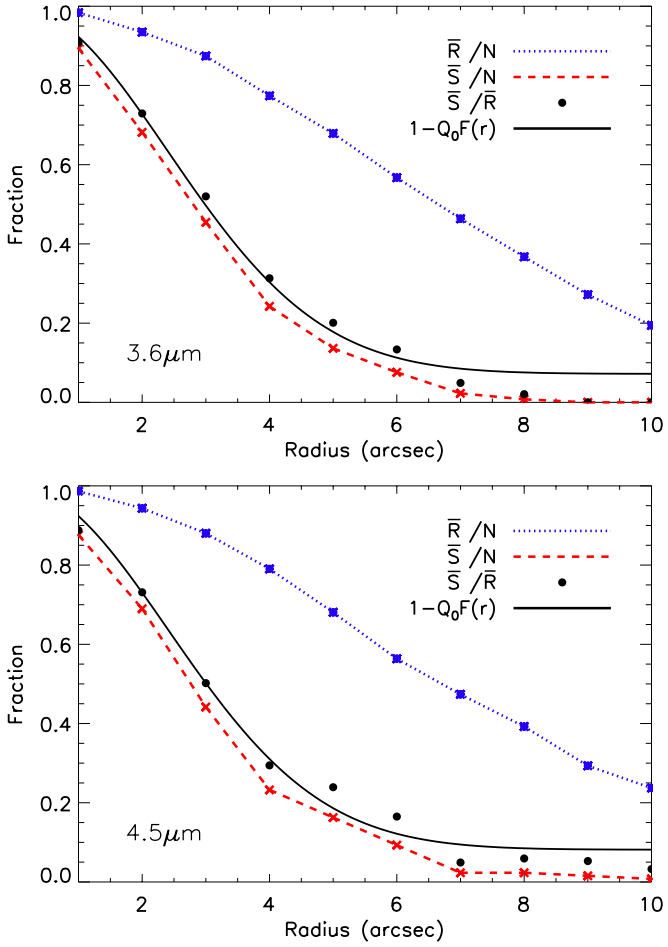

Figure 3. Quantities employed in the calculation of Q_0. $\bar{S}(r)/\bar{R}(r)$, the ratio of SPIRE blanks to random blanks, is fitted with $1 - Q_0 F(r)$ in order to calculate Q_0. The best-fit values are $Q_0 = 0.93 \pm 0.09$ and 0.92 ± 0.08 at 3.6 and 4.5 μm, respectively. We also show $\bar{R}(r)/N$ and $\bar{S}(r)/N$, the rate of random positions with at least one IRAC source and the rate of SPIRE blanks, respectively.
(A color version of this figure is available in the online journal.)

3.6 μm in IRAC. However, 79% of the 3.6 μm identified counterparts have $[3.6] \leqslant 19.7$ mag, suggesting that IRAC data to this depth would identify counterparts to ∼60% of SPIRE sources. The remaining difference in the IRAC and *WISE* identification rates is likely to be due to the resolutions of the instruments—the *WISE* 3.4 μm beam is ∼3 times larger than IRAC—although cosmic variance may also contribute. We note that if instead the data were limited to $[3.6] < 20.5$, corresponding to the 5σ point-source detection limit reached in a 120 s integration with IRAC at 3.6 μm, the expected identification rate drops from 77% to ∼70%.

The results presented here are insensitive to the exact value of Q_0. When using a 1σ lower value for Q_0 (i.e., $Q_0 = 0.84$ at both 3.6 and 4.5 μm), and comparing to the results presented in Section 3.3 and Table 2, the counterparts to 116 sources (95%) are unchanged. In this case there are four (3%) previously identified sources that no longer have reliable counterparts, and three (2%) previously unidentified SPIRE sources that now have $R \geqslant 0.8$ counterparts.

3.4. Counterparts Identified in IRAC Color–Magnitude Space

While we reliably identify 77% of the SPIRE sources with the LR method, the values of Q_0 indicate that ∼90% of SPIRE counterparts are detected in IRAC. Figure 4 shows the IRAC color–magnitude diagram for galaxies in the H-ATLAS SDP field, with SPIRE counterparts identified with the LR method highlighted. These galaxies occupy a distinct region of IRAC color–magnitude space—they typically have $[3.6] - [4.5] \gtrsim -0.4$ and are brighter than the background population. We use this property to identify counterparts to the SPIRE sources that have both 3.6 and 4.5 μm IRAC coverage but no $R \geqslant 0.8$ counterparts from the LR method. A similar analysis was performed by Biggs et al. (2011) at 3.6 and 5.8 μm to identify to LABOCA 870 μm sources.

We begin by determining the region of color–magnitude space in which there is a minimal chance of contamination by background sources (the ID region). A 20% contamination limit is used because this is equivalent to $R \geqslant 0.8$ for the LR method. We demarcate the ID region with the simplest reasonable function—a single diagonal line. The placement of the line is determined by calculating the gradients and intercepts that would yield 20% contamination from background sources within 7.″2 radius of the LR counterparts. The number of LR counterparts returned is maximized to yield a best-fit gradient of 0.515 for a line that intercepts $[3.6] = 16.0$ mag at $[3.6] - [4.5] = -2.142$. This division is shown as a solid line in Figure 4. IRAC galaxies that lie above this line and are within 7.″2 of SPIRE sources that are otherwise unidentified, have >80% probability of being physically associated with the SPIRE source, i.e., <20% chance of being an unrelated foreground or background galaxies, and are considered counterparts.

There are 36 SPIRE sources that do not have LR counterparts. Of these, 19 have both 3.6 and 4.5 μm data, and 23 IRAC counterparts to 13 of these sources are identified with the color–magnitude method (7 have multiple counterparts). These sources are presented in Table 2. The contamination rate for this method is 12.6% (approximately two IRAC galaxies), calculated

Table 2
Combined Photometry for IRAC IDs

IAU ID	H-ATLAS ID	R.A.[a] (J2000)	Decl.[a] (J2000)	Z[b] (mag)	Y[b] (mag)	J[b] (mag)	H[b] (mag)	K_s[b] (mag)	3.6 μm (mag)	4.5 μm (mag)	S_{250}[c] (mJy)	S_{350}[c] (mJy)	S_{500}[c] (mJy)	R[d] (3.6 μm)	R[d] (4.5 μm)	z[e]	Separation[f] (arcsec)
J090311.6+003906	81	09^{h}03^{m}11.57	+00°39′06.″4	18.80 ± 18.80	18.51 ± 0.02	18.25 ± 0.01	17.98 ± 0.01	17.68 ± 0.01	18.00 ± 0.01	18.03 ± 0.01	129.00 ± 6.56	181.86 ± 7.34	165.92 ± 9.27	1.000	0.999	0.30 ± 0.00	0.66
J090818.2+004720	106	09^{h}08^{m}18.31	+00°47′18.″9	20.59 ± 20.59	20.12 ± 0.04	20.08 ± 0.04	19.62 ± 0.06	19.00 ± 0.03	...	17.01 ± 0.01	116.93 ± 6.54	81.56 ± 7.40	27.71 ± 8.96	...	1.000	0.73 ± 0.20	1.80
J091304.9−005343	130	09^{h}08^{m}05.09	−00°53′43.″2	19.05 ± 19.05	18.78 ± 0.01	18.53 ± 0.01	18.25 ± 0.02	17.97 ± 0.01	18.10 ± 0.01	18.08 ± 0.01	105.04 ± 6.47	127.57 ± 7.21	107.52 ± 9.01	0.999	0.999	0.21 ± 0.02	2.23
J090918.3+002420	177	09^{h}09^{m}18.46	+00°24′21.″0	17.91 ± 17.91	17.72 ± 0.01	17.55 ± 0.01	17.29 ± 0.01	17.35 ± 0.01	17.55 ± 0.01	17.88 ± 0.01	107.24 ± 7.83	45.96 ± 7.20	3.88 ± 9.00	1.000	0.999	0.07 ± 0.00	1.43
J090916.1+003208	282	09^{h}09^{m}16.10	+00°32′07.″1	>23.06	>22.35	21.90 ± 0.19	20.81 ± 0.15	20.35 ± 0.12	19.01 ± 0.01	18.77 ± 0.01	81.47 ± 6.43	60.26 ± 7.13	33.18 ± 9.02	0.970	0.989	...	1.07
J090916.7+002808	317	09^{h}09^{m}16.82	+00°28′07.″8	21.44 ± 21.44	21.04 ± 0.06	20.47 ± 0.05	19.85 ± 0.06	19.15 ± 0.04	18.50 ± 0.01	18.78 ± 0.01	87.56 ± 6.45	64.38 ± 7.23	17.53 ± 9.02	0.998	0.999	...	0.51
J090835.8+004139	458	09^{h}08^{m}35.82	+00°41′40.″6	19.04 ± 19.04	18.80 ± 0.01	18.41 ± 0.01	18.02 ± 0.01	17.70 ± 0.01	17.97 ± 0.01	17.78 ± 0.01	75.75 ± 6.49	32.32 ± 7.13	10.83 ± 8.79	1.000	0.999	0.31 ± 0.05	0.81
J090930.4+002224	462*	09^{h}09^{m}30.51	+00°22′30.″8	19.54 ± 19.54	19.35 ± 0.02	19.05 ± 0.02	18.74 ± 0.02	18.48 ± 0.02	18.71 ± 0.01	18.76 ± 0.01	72.48 ± 6.36	76.71 ± 7.21	54.92 ± 8.92	0.121	0.159	0.13 ± 0.03	6.73
J090327.7+004119	466	09^{h}03^{m}27.65	+00°41′18.″1	18.68 ± 18.68	18.32 ± 0.01	18.17 ± 0.01	17.95 ± 0.01	17.86 ± 0.01	17.81 ± 0.01	18.04 ± 0.01	74.80 ± 6.50	33.52 ± 7.21	11.24 ± 9.00	0.999	0.871	0.13 ± 0.00	2.92
J090816.8+003211	493	09^{h}08^{m}16.90	+00°32′11.″6	>22.43	>22.02	21.77 ± 0.18	21.23 ± 0.25	20.78 ± 0.16	19.35 ± 0.01	18.85 ± 0.01	75.63 ± 6.54	61.45 ± 7.20	31.51 ± 9.16	0.997	0.999	...	0.77
J090829.1+002714	511	09^{h}08^{m}28.96	+00°27′12.″6	21.14 ± 21.14	20.76 ± 0.07	20.37 ± 0.05	19.92 ± 0.08	19.43 ± 0.05	18.53 ± 0.01	18.34 ± 0.01	72.97 ± 6.50	48.30 ± 7.14	31.77 ± 8.95	0.995	0.998	0.44 ± 0.10	3.50
J090925.3+004438	558	09^{h}09^{m}25.32	+00°44′37.″9	>22.54	>21.73	>21.05	>19.74	>19.13	...	20.37 ± 0.04	73.14 ± 6.54	65.94 ± 7.22	50.22 ± 9.10	...	0.960	...	0.81
J090828.0+005005	641	09^{h}08^{m}28.00	+00°50′04.″8	18.40 ± 18.40	18.34 ± 0.01	18.06 ± 0.01	17.84 ± 0.01	17.70 ± 0.01	...	17.96 ± 0.01	67.29 ± 6.53	28.12 ± 7.15	12.22 ± 8.95	...	0.999	0.17 ± 0.00	1.05
J090803.6+003737	711	09^{h}08^{m}03.55	+00°37′36.″7	19.59 ± 19.59	19.03 ± 0.02	19.13 ± 0.02	18.79 ± 0.03	18.51 ± 0.02	18.21 ± 0.01	18.27 ± 0.01	64.26 ± 6.51	36.95 ± 7.29	11.65 ± 9.15	0.999	0.999	0.26 ± 0.04	1.55
J090308.5+004146	754	09^{h}03^{m}08.55	+00°41′46.″0	...	...	...	...	...	19.98 ± 0.02	19.62 ± 0.02	65.99 ± 6.55	46.14 ± 7.25	28.08 ± 9.21	0.984	0.990	...	0.45
J090910.2+004345	776	09^{h}09^{m}10.35	+00°43′42.″1	...	...	...	...	...	...	20.10 ± 0.03	65.86 ± 6.44	51.68 ± 7.18	34.00 ± 8.98	...	0.926	...	4.11
J090844.0+003256	827*	09^{h}08^{m}44.06	+00°32′56.″7	...	...	...	...	...	19.82 ± 0.04	19.58 ± 0.03	61.63 ± 6.35	30.69 ± 7.27	19.89 ± 9.18	0.353	0.454	...	0.88
J090844.0+003256	827*	09^{h}08^{m}44.02	+00°33′00.″7	...	...	...	...	...	20.18 ± 0.04	20.07 ± 0.04	61.63 ± 6.35	30.69 ± 7.27	19.89 ± 9.18	0.055	0.065	...	3.88
J090844.0+003256	827*	09^{h}08^{m}44.28	+00°32′53.″9	19.29 ± 19.29	19.20 ± 0.02	18.89 ± 0.01	18.57 ± 0.02	18.25 ± 0.02	18.65 ± 0.01	18.68 ± 0.01	61.63 ± 6.35	30.69 ± 7.27	19.89 ± 9.18	0.109	0.170	0.20 ± 0.03	5.00
J090844.0+003256	827*	09^{h}08^{m}43.69	+00°32′57.″9	18.21 ± 18.21	18.04 ± 0.01	17.77 ± 0.01	17.50 ± 0.01	17.43 ± 0.01	17.85 ± 0.01	18.09 ± 0.01	61.63 ± 6.35	30.69 ± 7.27	19.89 ± 9.18	0.482	0.309	0.07 ± 0.01	4.91
J090929.1+002440	861	09^{h}09^{m}29.33	+00°24′42.″3	19.12 ± 19.12	18.96 ± 0.01	18.61 ± 0.01	18.31 ± 0.02	18.02 ± 0.02	18.09 ± 0.01	18.00 ± 0.01	63.93 ± 6.52	40.59 ± 7.21	20.48 ± 9.11	0.998	0.999	0.16 ± 0.02	3.02
J090814.6+002707	865	09^{h}08^{m}14.59	+00°27′04.″6	>22.43	21.91 ± 0.18	21.42 ± 0.13	20.75 ± 0.16	19.96 ± 0.08	19.21 ± 0.01	19.15 ± 0.01	60.43 ± 6.52	43.91 ± 7.40	15.89 ± 9.19	0.994	0.994	...	3.00
J090849.8+003203	891*	09^{h}08^{m}50.09	+00°32′02.″6	...	...	...	...	...	20.64 ± 0.03	20.26 ± 0.02	62.76 ± 6.48	75.75 ± 7.23	84.45 ± 9.07	0.407	0.437	...	3.21
J090849.8+003203	891*	09^{h}08^{m}50.06	+00°32′05.″2	...	...	...	...	...	20.73 ± 0.03	20.30 ± 0.03	62.76 ± 6.48	75.75 ± 7.23	84.45 ± 9.07	0.465	0.500	...	2.96
J090925.5+001941	946	09^{h}09^{m}25.44	+00°19′39.″6	21.63 ± 21.63	21.44 ± 0.09	21.47 ± 0.13	20.73 ± 0.14	20.49 ± 0.13	19.39 ± 0.01	19.43 ± 0.01	62.16 ± 6.45	29.23 ± 7.19	9.99 ± 8.83	0.901	0.916	...	2.34
J090800.6+002651	977	09^{h}08^{m}00.46	+00°26′51.″1	17.12 ± 17.12	16.81 ± 0.00	16.73 ± 0.00	16.52 ± 0.00	16.57 ± 0.00	16.87 ± 0.01	17.28 ± 0.01	58.89 ± 6.48	36.59 ± 7.19	12.91 ± 8.91	0.933	0.984	0.10 ± 0.00	3.52
J090856.6+003813	1147	09^{h}08^{m}56.63	+00°38′15.″3	20.05 ± 20.05	19.64 ± 0.03	19.38 ± 0.02	19.00 ± 0.03	18.56 ± 0.02	18.23 ± 0.01	18.08 ± 0.01	60.04 ± 6.34	34.84 ± 7.16	10.17 ± 9.03	0.940	0.955	0.32 ± 0.08	1.68
J090841.3+001559	1178	09^{h}08^{m}41.27	+00°15′59.″2	18.84 ± 18.84	18.89 ± 0.02	18.57 ± 0.01	18.31 ± 0.02	18.04 ± 0.01	18.28 ± 0.01	...	59.80 ± 6.40	35.59 ± 7.26	16.22 ± 8.96	0.999	...	0.20 ± 0.03	1.48
J090847.4+003459	1221	09^{h}08^{m}47.42	+00°35′05.″8	20.78 ± 20.78	20.48 ± 0.05	20.43 ± 0.05	20.08 ± 0.09	19.76 ± 0.06	19.81 ± 0.02	19.87 ± 0.03	55.73 ± 6.48	42.34 ± 7.16	26.26 ± 8.97	0.816	0.815	0.30 ± 0.09	6.77
J090920.5+004420	1248	09^{h}09^{m}20.45	+00°44′19.″5	16.90 ± 16.90	16.72 ± 0.00	16.50 ± 0.00	16.26 ± 0.00	16.35 ± 0.00	...	17.16 ± 0.01	56.25 ± 7.83	21.45 ± 7.24	25.88 ± 8.81	...	1.000	0.05 ± 0.00	1.47
J090932.7+003705	1264	09^{h}09^{m}32.77	+00°37′06.″8	22.32 ± 22.32	22.22 ± 0.18	21.34 ± 0.11	21.19 ± 0.21	20.55 ± 0.14	19.90 ± 0.02	20.08 ± 0.03	56.01 ± 6.47	40.49 ± 7.16	23.38 ± 8.97	0.787	0.717	...	1.58
J090824.5+002927	1288	09^{h}08^{m}24.84	+00°29′29.″4	>22.37	>22.02	21.56 ± 0.15	>20.99	20.31 ± 0.10	19.39 ± 0.01	19.22 ± 0.01	55.29 ± 6.54	46.57 ± 7.23	23.28 ± 9.01	0.988	0.989	...	4.08
J090913.6+003256	1293*	09^{h}09^{m}14.04	+00°32′59.″0	>22.54	>21.73	>21.05	>19.74	>19.13	20.48 ± 0.03	20.24 ± 0.02	55.08 ± 6.48	52.82 ± 7.22	36.26 ± 9.16	0.272	0.530	...	6.70
J090851.4+003955	1340	09^{h}08^{m}51.38	+00°39′54.″0	21.79 ± 21.79	21.35 ± 0.11	20.68 ± 0.07	20.27 ± 0.10	19.58 ± 0.05	18.78 ± 0.01	18.88 ± 0.01	53.96 ± 6.51	38.57 ± 7.21	9.59 ± 8.96	0.998	0.999	...	0.96
J090818.5+002043	1366	09^{h}08^{m}18.74	+00°20′40.″1	20.02 ± 20.02	19.68 ± 0.03	19.56 ± 0.03	19.21 ± 0.04	18.99 ± 0.03	19.06 ± 0.01	...	55.40 ± 6.46	31.22 ± 7.15	16.40 ± 9.04	0.888	...	0.21 ± 0.03	4.48
J090755.2+002254	1381	09^{h}07^{m}54.99	+00°22′55.″3	>22.37	21.87 ± 0.18	21.56 ± 0.15	21.04 ± 0.21	20.50 ± 0.12	19.54 ± 0.01	...	55.67 ± 6.39	39.10 ± 7.28	30.98 ± 9.13	0.969	...	...	4.05
J090845.7+002805	1397	09^{h}08^{m}45.88	+00°28′06.″0	21.47 ± 21.47	20.99 ± 0.08	21.31 ± 0.12	20.57 ± 0.14	20.12 ± 0.09	19.11 ± 0.01	18.97 ± 0.01	55.06 ± 6.60	44.21 ± 7.30	33.07 ± 9.01	0.996	0.998	0.50 ± 0.12	1.96
J090934.9+002840	1398*	09^{h}09^{m}34.57	+00°28′40.″3	22.26 ± 22.26	22.62 ± 0.26	21.63 ± 0.15	20.87 ± 0.16	20.65 ± 0.15	19.86 ± 0.02	19.93 ± 0.02	55.33 ± 6.56	44.18 ± 7.16	28.99 ± 9.06	0.346	0.366	...	5.33
J090934.9+002840	1398*	09^{h}09^{m}35.07	+00°28′43.″5	...	...	...	...	...	20.06 ± 0.02	20.02 ± 0.03	55.33 ± 6.56	44.18 ± 7.16	28.99 ± 9.06	0.637	0.615	...	3.77
J090817.7+002106	1426	09^{h}08^{m}17.68	+00°21′08.″3	22.36 ± 22.36	21.96 ± 0.19	21.77 ± 0.18	>20.99	20.52 ± 0.12	19.00 ± 0.01	...	54.34 ± 6.53	32.19 ± 7.14	13.61 ± 8.92	0.996	...	...	1.62
J090854.3+003248	1434	09^{h}08^{m}54.48	+00°32′48.″4	19.21 ± 19.21	19.02 ± 0.02	18.48 ± 0.01	18.00 ± 0.01	17.52 ± 0.01	17.85 ± 0.01	17.79 ± 0.01	47.07 ± 6.42	11.82 ± 7.16	2.31 ± 9.10	0.994	0.999	0.31 ± 0.08	1.33
J090924.3+004156	1483	09^{h}09^{m}24.32	+00°41′54.″3	...	...	...	...	...	...	20.06 ± 0.02	50.52 ± 6.42	36.97 ± 7.21	24.34 ± 8.95	...	0.987	...	2.20
J090945.6+003714	1559	09^{h}09^{m}45.59	+00°37′14.″1	...	...	...	...	...	19.56 ± 0.02	19.29 ± 0.01	53.50 ± 6.44	45.17 ± 7.24	39.72 ± 9.05	0.995	0.997	...	1.07
J090823.8+004611	1685	09^{h}08^{m}23.78	+00°46′10.″3	16.77 ± 16.77	16.78 ± 0.00	16.83 ± 0.00	16.95 ± 0.01	17.32 ± 0.01	18.36 ± 0.01	18.71 ± 0.01	53.11 ± 6.49	31.00 ± 7.12	21.12 ± 9.27	0.999	0.998	...	1.14
J090822.6+004200	1750	09^{h}08^{m}22.88	+00°42′04.″2	19.71 ± 19.71	19.33 ± 0.02	18.89 ± 0.01	18.45 ± 0.02	18.02 ± 0.01	18.38 ± 0.01	18.38 ± 0.01	51.85 ± 6.51	36.36 ± 7.26	21.11 ± 8.90	0.913	0.985	0.14 ± 0.02	5.47
J090307.6+004012	1762	09^{h}03^{m}07.79	+00°40′16.″7	20.23 ± 20.23	19.91 ± 0.05	19.74 ± 0.03	19.28 ± 0.03	18.89 ± 0.03	18.82 ± 0.01	19.03 ± 0.01	53.54 ± 6.56	49.59 ± 7.17	33.94 ± 8.91	0.990	0.983	...	4.62
J090920.4+002316	1976	09^{h}09^{m}20.46	+00°23′21.″1	20.14 ± 20.14	19.95 ± 0.03	19.51 ± 0.02	18.91 ± 0.03	18.44 ± 0.02	18.48 ± 0.01	18.36 ± 0.01	50.05 ± 6.57	23.40 ± 7.29	11.60 ± 9.11	0.940	0.948	0.45 ± 0.07	4.91
J090314.5+003359	2121	09^{h}03^{m}14.73	+00°33′58.″6	18.95 ± 18.95	18.88 ± 0.02	18.67 ± 0.01	18.30 ± 0.02	18.04 ± 0.01	18.37 ± 0.01	...	48.57 ± 6.51	17.97 ± 7.26	12.58 ± 8.86	0.999	...	0.23 ± 0.04	2.60
J090920.5+003742	2180	09^{h}09^{m}20.31	+00°37′42.″5	18.97 ± 18.97	18.74 ± 0.01	18.39 ± 0.01	18.05 ± 0.01	17.77 ± 0.01	18.13 ± 0.01	18.27 ± 0.01	48.41 ± 6.43	49.96 ± 7.18	44.04 ± 8.93	0.998	0.998	0.30 ± 0.05	3.13
J090913.5+002736	2244	09^{h}09^{m}13.54	+00°27′33.″9	...	...	...	...	...	19.02 ± 0.01	19.28 ± 0.01	48.09 ± 6.51	39.94 ± 7.22	32.63 ± 9.21	0.993	0.994	...	3.08
J090855.6+001526	2277	09^{h}08^{m}55.92	+00°15′25.″2	18.98 ± 18.98	18.77 ± 0.01	18.35 ± 0.01	18.02 ± 0.01	17.75 ± 0.01	17.94 ± 0.01	...	46.36 ± 6.47	16.00 ± 7.20	-2.30 ± 9.00	0.998	...	0.20 ± 0.04	4.56

Table 2
(Continued)

IAU ID	H-ATLAS ID	R.A.[a] (J2000)	Decl.[a] (J2000)	Z[b] (mag)	Y[b] (mag)	J[b] (mag)	H[b] (mag)	K_s[b] (mag)	3.6 μm (mag)	4.5 μm (mag)	S_{250}[c] (mJy)	S_{350}[c] (mJy)	S_{500}[c] (mJy)	R[d] (3.6 μm)	R[d] (4.5 μm)	z[e]	Separation[f] (arcsec)
J090925.2+003224	2281	09^{m}09^{h}25^s.11	+00°32′26″.8	>23.06	>22.35	21.43 ± 0.12	20.87 ± 0.16	20.32 ± 0.11	19.39 ± 0.01	19.04 ± 0.01	47.80 ± 6.50	41.33 ± 7.27	14.29 ± 9.27	0.992	0.993	...	3.35
J091257.8−005508	2343	09^{m}09^{h}57^s.82	−00°55′02″.7	18.46 ± 18.46	18.13 ± 0.01	17.98 ± 0.01	17.91 ± 0.01	18.08 ± 0.02	18.22 ± 0.01	18.28 ± 0.01	42.07 ± 6.55	24.56 ± 7.29	10.37 ± 9.30	0.927	0.949	0.38 ± 0.07	5.75
J090841.3+002005	2432	09^{m}08^{h}41^s.38	+00°20′06″.6	20.27 ± 20.27	19.97 ± 0.03	19.79 ± 0.03	19.25 ± 0.04	18.80 ± 0.03	18.70 ± 0.01	...	46.36 ± 6.45	27.64 ± 7.15	30.30 ± 9.12	0.998	...	0.39 ± 0.07	1.44
J090752.3+002100	2437	09^{m}07^{h}52^s.22	+00°21′00″.3	...	...	...	...	...	20.05 ± 0.02	...	46.26 ± 6.46	34.17 ± 7.25	20.42 ± 9.32	0.989	...	...	1.92
J090850.0+004309	2459*	09^{m}08^{h}49^s.79	+00°43′07″.7	20.62 ± 20.62	20.11 ± 0.04	20.02 ± 0.04	19.56 ± 0.05	19.16 ± 0.04	18.80 ± 0.01	18.81 ± 0.01	46.74 ± 6.55	30.97 ± 7.16	6.70 ± 8.99	0.354	0.399	...	4.45
J090850.0+004309	2459*	09^{m}08^{h}50^s.16	+00°43′09″.7	>22.37	21.98 ± 0.20	22.17 ± 0.26	21.09 ± 0.22	20.61 ± 0.14	19.76 ± 0.03	19.65 ± 0.01	46.74 ± 6.55	30.97 ± 7.16	6.70 ± 8.99	0.643	0.598	...	1.50
J090803.8+002250	2549	09^{m}08^{h}03^s.57	+00°22′51″.6	19.52 ± 19.52	18.90 ± 0.02	18.62 ± 0.01	18.18 ± 0.02	17.83 ± 0.01	18.12 ± 0.01	...	45.96 ± 6.55	23.21 ± 7.15	2.63 ± 9.01	0.995	...	0.29 ± 0.08	4.67
J090855.5+002808	2565	09^{m}08^{h}55^s.59	+00°28′06″.8	>21.79	>21.40	>20.94	> − 99.00	>19.20	21.25 ± 0.06	20.83 ± 0.04	45.75 ± 6.51	38.65 ± 7.14	32.42 ± 8.92	0.896	0.977	...	1.85
J090930.2+002755	2680	09^{m}09^{h}30^s.22	+00°27′55″.0	22.07 ± 22.07	21.55 ± 0.10	20.99 ± 0.08	20.49 ± 0.11	20.08 ± 0.09	19.27 ± 0.01	19.21 ± 0.01	45.12 ± 6.36	37.32 ± 7.15	15.07 ± 8.93	0.953	0.966	...	0.51
J090803.7+002921	2715	09^{m}08^{h}03^s.82	+00°29′22″.6	>21.91	>21.40	>20.94	>19.61	>19.20	20.85 ± 0.04	20.39 ± 0.03	46.08 ± 6.52	28.66 ± 7.30	29.26 ± 9.02	0.985	0.990	...	1.14
J090905.3+001525	2773	09^{m}09^{h}05^s.49	+00°15′23″.6	>22.54	>21.73	>21.05	>19.74	>19.20	20.06 ± 0.02	...	44.96 ± 6.53	38.06 ± 7.18	25.49 ± 8.90	0.836	...	...	2.61
J090846.0+004339	2793*	09^{m}08^{h}46^s.01	+00°43′36″.8	...	...	...	...	...	20.41 ± 0.06	20.21 ± 0.03	45.21 ± 6.42	39.54 ± 7.23	18.88 ± 8.97	0.613	0.478	...	2.57
J090846.0+004339	2793*	09^{m}08^{h}45^s.88	+00°43′39″.0	...	...	...	...	...	20.56 ± 0.07	20.08 ± 0.02	45.21 ± 6.42	39.54 ± 7.23	18.88 ± 8.97	0.378	0.515	...	2.40
J090943.0+004322	2796	09^{m}09^{h}43^s.23	+00°43′22″.2	>23.06	>22.35	19.70 ± 0.03	19.38 ± 0.04	19.09 ± 0.04	...	18.66 ± 0.01	39.85 ± 6.38	21.33 ± 7.15	11.52 ± 9.10	...	0.998	0.16 ± 0.17	2.24
J090819.6+003259	2866	09^{m}08^{h}20^s.00	+00°33′02″.6	>22.43	>22.02	21.94 ± 0.21	>20.99	20.84 ± 0.17	19.95 ± 0.02	19.63 ± 0.01	44.81 ± 6.48	44.94 ± 7.15	34.21 ± 9.12	0.882	0.881	...	6.31
J091302.7−004618	2986	09^{m}08^{h}02^s.92	−00°46′19″.7	19.06 ± 19.06	18.85 ± 0.02	18.62 ± 0.01	18.39 ± 0.02	18.11 ± 0.02	...	18.22 ± 0.01	44.02 ± 6.53	21.20 ± 7.40	9.62 ± 8.99	...	0.928	0.25 ± 0.03	3.57
J090922.4+002715	3043	09^{m}09^{h}22^s.19	+00°27′15″.3	21.11 ± 21.11	20.80 ± 0.05	20.49 ± 0.05	20.15 ± 0.08	19.54 ± 0.06	18.87 ± 0.01	19.20 ± 0.01	42.74 ± 6.48	17.48 ± 7.14	14.55 ± 8.99	0.922	0.919	0.68 ± 0.12	3.57
J090333.3+004746	3056	09^{m}03^{h}33^s.53	+00°47′48″.8	...	...	...	...	...	...	19.44 ± 0.03	43.97 ± 6.43	48.32 ± 7.15	25.88 ± 8.83	...	0.891	...	3.12
J090800.5+002457	3084	09^{m}08^{h}00^s.51	+00°24′57″.3	>21.85	>21.40	>20.94	>19.61	>19.20	21.21 ± 0.05	...	42.94 ± 6.51	61.39 ± 7.18	46.14 ± 8.76	0.918	...	...	0.57
J090839.4+004107	3113	09^{m}08^{h}39^s.11	+00°41′06″.9	18.76 ± 18.76	18.39 ± 0.01	17.98 ± 0.01	17.57 ± 0.01	17.22 ± 0.01	17.62 ± 0.01	17.68 ± 0.01	44.18 ± 6.41	19.63 ± 7.23	-0.42 ± 9.33	0.959	0.948	0.25 ± 0.03	5.73
J090746.7+002148	3161	09^{m}07^{h}46^s.38	+00°21′47″.2	19.63 ± 19.63	19.24 ± 0.02	19.05 ± 0.02	18.64 ± 0.02	18.32 ± 0.02	18.52 ± 0.01	...	44.71 ± 6.44	18.68 ± 7.27	9.49 ± 9.12	0.984	...	0.35 ± 0.03	5.16
J090832.7+002406	3205	09^{m}08^{h}32^s.85	+00°24′07″.1	21.17 ± 21.17	20.64 ± 0.06	20.19 ± 0.04	19.64 ± 0.06	19.11 ± 0.04	18.65 ± 0.01	18.94 ± 0.01	40.89 ± 6.65	30.78 ± 7.31	14.69 ± 8.98	0.998	0.998	0.63 ± 0.10	2.13
J090829.1+001556	3242	09^{m}08^{h}28^s.96	+00°15′58″.8	>22.37	>22.02	21.90 ± 0.20	>20.99	20.49 ± 0.12	19.29 ± 0.02	...	42.99 ± 6.59	43.26 ± 7.16	15.88 ± 8.91	0.987	...	...	4.12
J090843.7+001437	3251	09^{m}08^{h}43^s.61	+00°14′38″.4	19.81 ± 19.81	19.59 ± 0.03	19.28 ± 0.02	18.82 ± 0.03	18.46 ± 0.02	18.20 ± 0.01	...	38.04 ± 6.61	28.16 ± 7.14	5.02 ± 8.95	0.961	...	0.51 ± 0.12	2.68
J091303.6−004855	3285	09^{m}08^{h}03^s.34	−00°48′59″.1	18.82 ± 18.82	18.58 ± 0.01	18.24 ± 0.01	17.92 ± 0.01	17.67 ± 0.01	...	18.20 ± 0.01	42.06 ± 6.40	11.54 ± 7.16	9.00 ± 9.00	...	0.975	0.11 ± 0.02	6.28
J090836.4+002948	3304	09^{m}08^{h}36^s.62	+00°29′48″.3	21.90 ± 21.90	21.38 ± 0.12	21.04 ± 0.09	20.94 ± 0.19	20.43 ± 0.11	19.22 ± 0.01	19.15 ± 0.01	39.87 ± 6.41	45.74 ± 7.28	31.52 ± 8.86	0.996	0.996	...	2.10
J090940.3+002939	3318	09^{m}09^{h}40^s.28	+00°29′42″.4	...	...	...	...	...	20.56 ± 0.04	20.33 ± 0.03	42.01 ± 6.55	32.10 ± 7.21	20.21 ± 8.92	0.932	0.985	...	2.56
J090921.9+002556	3457	09^{m}09^{h}21^s.78	+00°25′57″.6	18.83 ± 18.83	18.59 ± 0.01	18.20 ± 0.01	17.80 ± 0.01	17.53 ± 0.01	17.76 ± 0.01	17.92 ± 0.01	41.50 ± 6.41	19.09 ± 7.30	-12.39 ± 9.13	0.997	0.996	0.12 ± 0.02	2.33
J090832.2+001938	3573	09^{m}08^{h}32^s.24	+00°19′40″.5	18.93 ± 18.93	18.84 ± 0.01	18.48 ± 0.01	18.20 ± 0.02	17.94 ± 0.01	18.22 ± 0.01	...	41.25 ± 6.53	22.19 ± 7.17	1.67 ± 9.10	0.967	...	0.21 ± 0.03	2.15
J090323.9+004620	3574	09^{m}03^{h}23^s.60	+00°46′23″.8	19.83 ± 19.83	19.59 ± 0.03	19.33 ± 0.02	18.95 ± 0.03	18.66 ± 0.02	...	18.99 ± 0.01	41.37 ± 6.53	20.20 ± 7.25	9.76 ± 8.79	...	0.976	0.29 ± 0.07	5.75
J091317.7−004621	3583	09^{m}03^{h}17^s.75	−00°46′16″.1	19.94 ± 19.94	19.69 ± 0.03	19.61 ± 0.03	19.30 ± 0.04	18.98 ± 0.03	...	19.24 ± 0.01	41.18 ± 6.55	34.52 ± 7.14	20.07 ± 9.18	...	0.963	0.25 ± 0.05	5.53
J090901.5+003107	3616	09^{m}09^{h}01^s.77	+00°31′08″.1	21.55 ± 21.55	21.01 ± 0.08	20.54 ± 0.06	19.82 ± 0.07	19.17 ± 0.04	18.69 ± 0.01	19.05 ± 0.01	41.09 ± 6.50	20.53 ± 7.20	-1.89 ± 8.79	0.983	0.975	0.59 ± 0.08	2.59
J090858.8+003158	3714	09^{m}08^{h}58^s.82	+00°31′54″.8	20.47 ± 20.47	20.17 ± 0.04	19.86 ± 0.03	19.27 ± 0.04	18.95 ± 0.03	19.09 ± 0.01	19.04 ± 0.01	39.63 ± 6.46	15.19 ± 7.24	-3.99 ± 8.95	0.882	0.944	0.53 ± 0.08	3.62
J091001.4+004024	3792	09^{m}08^{h}01^s.44	+00°40′21″.8	21.29 ± 21.29	21.16 ± 0.07	20.61 ± 0.06	20.22 ± 0.09	19.73 ± 0.07	...	19.56 ± 0.04	39.95 ± 6.38	28.10 ± 7.18	10.01 ± 9.26	...	0.984	0.46 ± 0.18	3.02
J090903.5+002031	3825	09^{m}09^{h}03^s.34	+00°20′30″.8	18.27 ± 18.27	18.09 ± 0.01	17.80 ± 0.01	17.52 ± 0.01	17.48 ± 0.01	17.43 ± 0.01	17.76 ± 0.01	38.19 ± 6.48	12.71 ± 7.23	5.37 ± 9.19	0.999	0.999	0.09 ± 0.00	3.02
J090921.9+004307	3974	09^{m}09^{h}22^s.24	+00°43′08″.3	>23.06	>22.35	20.60 ± 0.06	20.12 ± 0.08	19.73 ± 0.07	...	18.09 ± 0.01	40.61 ± 6.49	36.92 ± 7.22	23.08 ± 8.92	...	0.963	...	4.03
J090901.9+004217	4113	09^{m}09^{h}01^s.87	+00°42′19″.9	>23.06	>22.35	21.64 ± 0.16	>21.13	20.70 ± 0.15	19.80 ± 0.03	19.48 ± 0.01	37.23 ± 6.49	44.93 ± 7.14	32.16 ± 8.77	0.974	0.986	...	2.22
J090811.9+003410	4185	09^{m}08^{h}12^s.06	+00°34′13″.2	>22.43	>22.02	22.11 ± 0.25	>20.99	20.91 ± 0.18	19.94 ± 0.02	19.79 ± 0.02	39.10 ± 6.41	27.54 ± 7.22	27.09 ± 9.20	0.987	0.987	...	3.67
J090821.6+002700	4344	09^{m}08^{h}21^s.24	+00°27′00″.0	21.66 ± 21.66	21.42 ± 0.12	21.41 ± 0.13	>20.99	20.65 ± 0.14	19.73 ± 0.01	19.93 ± 0.02	38.39 ± 6.40	30.19 ± 7.18	20.33 ± 8.92	0.890	0.889	...	6.24
J090935.1+002224	4352	09^{m}09^{h}35^s.26	+00°22′22″.3	...	...	...	...	...	19.48 ± 0.03	19.47 ± 0.04	37.71 ± 6.61	26.04 ± 7.17	24.95 ± 9.08	0.983	0.986	...	2.79
J090918.3+003409	4366*	09^{m}09^{h}18^s.30	+00°34′09″.2	...	...	...	...	...	19.96 ± 0.02	19.73 ± 0.02	38.79 ± 6.55	31.27 ± 7.24	14.04 ± 8.90	0.545	0.545	...	0.64
J090918.3+003409	4366*	09^{m}09^{h}18^s.44	+00°34′09″.7	20.82 ± 20.82	20.58 ± 0.04	20.50 ± 0.05	20.25 ± 0.09	19.99 ± 0.08	19.91 ± 0.02	19.87 ± 0.02	38.79 ± 6.55	31.27 ± 7.24	14.04 ± 8.90	0.452	0.452	0.46 ± 0.15	1.60
J091306.9−004719	4404	09^{m}09^{h}07^s.08	−00°47′20″.9	22.65 ± 22.65	22.23 ± 0.26	21.50 ± 0.16	20.84 ± 0.18	20.28 ± 0.10	...	19.11 ± 0.01	37.63 ± 6.52	32.91 ± 7.19	29.28 ± 9.11	...	0.996	...	2.37
J091318.1−005409	4520	09^{m}09^{h}18^s.11	−00°54′16″.1	21.98 ± 21.98	21.85 ± 0.18	21.56 ± 0.17	20.99 ± 0.20	20.74 ± 0.16	20.36 ± 0.04	20.83 ± 0.07	39.29 ± 6.62	20.79 ± 7.25	4.80 ± 9.07	0.764	0.590	...	6.51
J090744.7+002005	4524	09^{m}07^{h}44^s.70	+00°20′06″.0	>21.86	>21.40	>20.94	>19.61	>19.20	21.32 ± 0.10	...	37.82 ± 6.46	33.80 ± 7.11	19.53 ± 9.10	0.892	...	...	1.98
J090902.0+001936	4587*	09^{m}09^{h}02^s.05	+00°19′34″.2	...	...	...	...	...	21.36 ± 0.08	20.72 ± 0.10	34.85 ± 6.33	45.90 ± 7.21	32.27 ± 8.92	0.075	0.326	...	2.35
J090902.0+001936	4587*	09^{m}09^{h}02^s.39	+00°19′35″.2	21.32 ± 21.32	21.16 ± 0.09	20.56 ± 0.06	20.36 ± 0.11	19.84 ± 0.07	19.27 ± 0.01	19.63 ± 0.04	34.85 ± 6.33	45.90 ± 7.21	32.27 ± 8.92	0.357	0.219	0.33 ± 0.15	5.15
J090902.0+001936	4587*	09^{m}09^{h}01^s.94	+00°19′39″.3	...	...	...	...	...	20.27 ± 0.03	20.12 ± 0.05	34.85 ± 6.33	45.90 ± 7.21	32.27 ± 8.92	0.557	0.445	...	3.19
J091304.1−005141	4658	09^{m}09^{h}04^s.37	−00°51′42″.1	20.22 ± 20.22	19.94 ± 0.04	19.55 ± 0.03	19.08 ± 0.04	18.67 ± 0.02	18.73 ± 0.01	18.95 ± 0.01	37.35 ± 6.50	12.10 ± 7.18	8.14 ± 9.29	0.996	0.997	0.41 ± 0.04	3.12
J090851.6+003823	4693	09^{m}08^{h}51^s.66	+00°38′22″.3	...	...	...	...	...	20.21 ± 0.03	19.95 ± 0.03	38.05 ± 6.62	23.97 ± 7.16	3.68 ± 9.22	0.950	0.926	...	1.25
J090855.2+003051	4739	09^{m}08^{h}55^s.08	+00°30′50″.7	20.16 ± 20.16	19.88 ± 0.03	19.69 ± 0.03	19.29 ± 0.04	18.96 ± 0.03	18.96 ± 0.01	19.19 ± 0.01	37.35 ± 6.56	17.17 ± 7.17	6.70 ± 9.03	0.997	0.995	0.27 ± 0.06	2.60
J090842.2+001815	4779	09^{m}08^{h}42^s.51	+00°18′18″.2	19.72 ± 19.72	19.66 ± 0.03	19.36 ± 0.02	19.01 ± 0.03	18.69 ± 0.02	18.84 ± 0.01	...	37.31 ± 6.54	20.36 ± 7.18	15.89 ± 9.04	0.953	...	0.36 ± 0.07	5.10

Table 2
(Continued)

IAU ID	H-ATLAS ID	R.A.[a] (J2000)	Decl.[a] (J2000)	Z[b] (mag)	Y[b] (mag)	J[b] (mag)	H[b] (mag)	K_s[b] (mag)	3.6 μm (mag)	4.5 μm (mag)	S_{250}[c] (mJy)	S_{350}[c] (mJy)	S_{500}[c] (mJy)	R[d] (3.6 μm)	R[d] (4.5 μm)	z[e]	Separation[f] (arcsec)
J090831.3+002251	4849	09^{m}08^{h}31^s.31	+00°22′48.″2	21.08 ± 21.08	20.85 ± 0.07	20.29 ± 0.05	20.04 ± 0.08	19.51 ± 0.05	19.04 ± 0.01	19.39 ± 0.03	36.15 ± 6.53	30.24 ± 7.21	10.68 ± 8.78	0.939	0.983	0.51 ± 0.16	3.41
J090833.9+004616	4850	09^{m}08^{h}33^s.93	+00°46′16.″8	21.31 ± 21.31	21.01 ± 0.08	20.93 ± 0.08	20.16 ± 0.09	19.66 ± 0.06	...	18.60 ± 0.01	36.38 ± 6.55	33.06 ± 7.31	4.89 ± 9.28	...	0.999	...	0.90
J090847.1+003247	4930	09^{m}08^{h}47^s.07	+00°32′45.″8	17.50 ± 17.50	17.34 ± 0.01	17.03 ± 0.00	16.75 ± 0.01	16.54 ± 0.00	16.53 ± 0.01	16.33 ± 0.01	37.94 ± 6.53	22.44 ± 7.24	15.05 ± 8.92	0.998	...	0.16 ± 0.02	1.36
J090931.4+003936	5050	09^{m}09^{h}31^s.53	+00°39′38.″1	...	...	...	...	...	>23.00	20.07 ± 0.05	37.04 ± 6.55	41.24 ± 7.23	28.78 ± 8.89	...	0.989	...	1.61
J090741.5+002103	5082	09^{m}07^{h}41^s.34	+00°21′02.″8	21.07 ± 21.07	20.64 ± 0.06	20.39 ± 0.05	19.96 ± 0.08	19.64 ± 0.06	19.03 ± 0.01	...	36.51 ± 6.48	23.21 ± 7.30	21.40 ± 9.24	0.973	...	0.68 ± 0.15	3.92
J090757.3+003006	5157•	09^{m}07^{h}57^s.73	+00°30′05.″0	21.44 ± 21.44	21.01 ± 0.08	20.94 ± 0.09	20.41 ± 0.12	20.15 ± 0.09	19.30 ± 0.01	19.63 ± 0.02	35.18 ± 6.51	40.62 ± 7.21	30.04 ± 9.12	0.462	0.277	0.52 ± 0.12	5.43
J090846.2+004110	5258	09^{m}08^{h}46^s.38	+00°41′11.″0	20.03 ± 20.03	19.67 ± 0.03	19.28 ± 0.02	18.81 ± 0.03	18.40 ± 0.02	18.57 ± 0.01	18.51 ± 0.01	35.60 ± 6.57	17.51 ± 7.16	-4.48 ± 9.17	0.998	0.998	0.19 ± 0.03	1.79
J090938.9+003240	5267	09^{m}09^{h}39^s.00	+00°32′40.″5	20.07 ± 20.07	19.82 ± 0.02	19.58 ± 0.02	19.15 ± 0.03	18.89 ± 0.03	18.61 ± 0.01	18.99 ± 0.01	35.90 ± 6.55	18.28 ± 7.24	16.48 ± 9.06	0.971	0.983	0.59 ± 0.09	1.49
J090840.6+001725	5327	09^{m}08^{h}40^s.92	+00°17′24.″8	19.27 ± 19.27	19.19 ± 0.02	18.82 ± 0.01	18.54 ± 0.02	18.29 ± 0.02	18.58 ± 0.01	...	34.91 ± 6.27	19.10 ± 7.14	2.43 ± 9.07	0.935	...	0.20 ± 0.03	3.56
J090759.7+002033	5366	09^{m}07^{h}59^s.67	+00°20′34.″9	21.73 ± 21.73	21.39 ± 0.12	21.12 ± 0.10	20.86 ± 0.18	20.32 ± 0.10	19.49 ± 0.01	...	36.61 ± 6.37	19.92 ± 7.26	2.40 ± 9.03	0.996	...	...	1.49
J090932.9+002242	5386	09^{m}09^{h}33^s.01	+00°22′45.″6	...	...	...	...	...	21.38 ± 0.09	20.54 ± 0.05	34.12 ± 6.43	39.10 ± 7.26	27.32 ± 8.96	0.824	0.958	...	3.23
J090314.0+004235	5422	09^{m}03^{h}13^s.98	+00°42′31.″2	19.61 ± 19.61	19.39 ± 0.02	19.20 ± 0.02	19.00 ± 0.03	18.78 ± 0.03	18.97 ± 0.01	18.94 ± 0.01	33.19 ± 6.55	32.95 ± 7.19	4.46 ± 8.98	0.981	0.995	0.24 ± 0.04	3.85
J090914.8+002041	5450	09^{m}09^{h}14^s.82	+00°20′39.″5	21.62 ± 21.62	21.43 ± 0.09	21.07 ± 0.09	20.62 ± 0.13	20.47 ± 0.13	20.46 ± 0.03	20.85 ± 0.05	35.94 ± 6.42	24.72 ± 7.23	16.42 ± 9.06	0.987	0.922	0.39 ± 0.19	2.44
J090929.6+003313	5521	09^{m}09^{h}29^s.72	+00°33′16.″2	>22.54	>21.73	>21.05	>19.74	>19.13	19.64 ± 0.01	19.43 ± 0.01	35.71 ± 6.31	24.72 ± 7.15	8.91 ± 8.99	0.992	0.995	...	2.75
J090837.1+005002	5530	09^{m}08^{h}37^s.04	+00°50′02.″2	20.91 ± 20.91	20.67 ± 0.06	20.10 ± 0.04	19.72 ± 0.06	19.21 ± 0.04	...	18.17 ± 0.01	36.26 ± 6.56	16.39 ± 7.27	-0.12 ± 9.02	...	0.999	0.60 ± 0.06	0.93
J090825.8+004217	5538	09^{m}08^{h}25^s.83	+00°42′13.″7	22.80 ± 22.80	22.16 ± 0.23	21.76 ± 0.18	21.21 ± 0.24	20.68 ± 0.14	20.32 ± 0.03	20.77 ± 0.03	35.38 ± 6.41	17.99 ± 7.32	-5.24 ± 9.06	0.736	0.661	...	3.46
J090821.9+002445	5564	09^{m}08^{h}22^s.14	+00°24′47.″3	>22.37	22.06 ± 0.21	21.45 ± 0.13	20.77 ± 0.16	20.13 ± 0.09	19.30 ± 0.01	19.18 ± 0.01	35.10 ± 6.62	19.57 ± 7.16	7.32 ± 8.97	0.992	0.993	...	3.29
J090910.9+003517	5621	09^{m}09^{h}11^s.35	+00°35′17.″4	20.81 ± 20.81	20.71 ± 0.05	20.34 ± 0.05	20.13 ± 0.08	19.66 ± 0.06	18.97 ± 0.01	19.22 ± 0.01	33.80 ± 6.56	25.47 ± 7.15	26.89 ± 8.96	0.973	0.956	0.71 ± 0.11	5.72
J090848.1+002626	5691	09^{m}08^{h}48^s.13	+00°26′22.″1	20.10 ± 20.10	19.89 ± 0.03	19.57 ± 0.03	19.19 ± 0.04	18.86 ± 0.03	19.04 ± 0.01	19.29 ± 0.01	35.24 ± 6.38	18.50 ± 7.16	16.50 ± 8.90	0.885	0.890	0.39 ± 0.05	4.15
J090812.1+002430	5735	09^{m}08^{h}12^s.26	+00°24′30.″7	19.21 ± 19.21	18.78 ± 0.01	18.66 ± 0.01	18.45 ± 0.02	18.16 ± 0.02	18.31 ± 0.01	18.21 ± 0.01	34.91 ± 6.51	15.87 ± 7.25	3.13 ± 8.99	0.998	0.997	0.16 ± 0.02	1.00
J090852.9+004106	5774	09^{m}08^{h}52^s.90	+00°41′07.″1	>21.85	>21.40	>20.94	>19.61	>19.20	19.82 ± 0.02	19.58 ± 0.01	33.83 ± 6.45	38.19 ± 7.17	22.59 ± 9.26	0.996	0.996	...	0.79
J090912.3+002129	6012	09^{m}09^{h}12^s.65	+00°21′28.″0	19.82 ± 19.82	19.59 ± 0.02	19.27 ± 0.02	18.90 ± 0.03	18.63 ± 0.03	18.38 ± 0.01	18.81 ± 0.01	35.13 ± 6.65	24.35 ± 7.22	6.36 ± 9.07	0.997	0.995	0.56 ± 0.02	3.93
J090908.3+002545	6100•	09^{m}09^{h}08^s.64	+00°25′48.″4	22.45 ± 22.45	21.84 ± 0.13	21.55 ± 0.14	21.16 ± 0.21	20.48 ± 0.13	19.52 ± 0.01	19.35 ± 0.01	33.08 ± 6.38	44.67 ± 7.17	42.48 ± 8.86	0.244	0.540	...	4.78
J090902.6+004737	6146	09^{m}09^{h}02^s.42	+00°47′39.″5	21.63 ± 21.63	21.56 ± 0.13	20.92 ± 0.08	20.48 ± 0.12	19.89 ± 0.07	...	19.58 ± 0.01	32.24 ± 6.37	20.07 ± 7.18	2.26 ± 8.98	...	0.976	0.66 ± 0.22	4.49
J090928.7+002630	6189•	09^{m}09^{h}29^s.03	+00°26′31.″0	>22.54	>21.73	>21.05	>19.74	>19.13	20.90 ± 0.05	20.48 ± 0.03	33.47 ± 6.52	35.08 ± 7.28	35.56 ± 8.97	0.302	0.430	...	4.06
J090754.6+003345	6220•	09^{m}07^{h}54^s.82	+00°33′42.″2	19.71 ± 19.71	19.41 ± 0.02	19.14 ± 0.02	18.79 ± 0.03	18.48 ± 0.02	18.68 ± 0.01	18.77 ± 0.01	34.05 ± 6.51	12.37 ± 7.23	8.23 ± 9.14	0.518	0.570	0.19 ± 0.04	4.19
J090946.4+003847	6224	09^{m}09^{h}46^s.39	+00°38′47.″1	20.48 ± 20.48	20.19 ± 0.03	19.83 ± 0.03	19.25 ± 0.04	18.81 ± 0.03	18.65 ± 0.02	18.76 ± 0.01	34.77 ± 6.59	14.14 ± 7.24	4.09 ± 9.06	0.998	0.999	0.46 ± 0.12	0.97
J090832.0+002749	6324	09^{m}08^{h}31^s.94	+00°27′52.″4	22.04 ± 22.04	21.85 ± 0.17	21.59 ± 0.15	20.77 ± 0.16	20.22 ± 0.10	19.18 ± 0.01	19.21 ± 0.01	33.98 ± 6.35	23.50 ± 7.19	10.73 ± 9.12	0.989	0.972	...	2.90
J090956.0+003739	6348	09^{m}09^{h}56^s.03	+00°37′37.″2	19.46 ± 19.46	19.18 ± 0.02	18.77 ± 0.01	18.31 ± 0.02	17.86 ± 0.01	18.22 ± 0.01	18.18 ± 0.01	33.90 ± 6.45	12.66 ± 7.24	-3.81 ± 9.38	0.999	0.999	0.28 ± 0.06	2.12
J090840.1+001928	6480	09^{m}08^{h}40^s.02	+00°19′30.″1	19.88 ± 19.88	19.80 ± 0.03	19.50 ± 0.02	19.37 ± 0.05	19.03 ± 0.03	19.25 ± 0.01	...	33.32 ± 6.55	25.13 ± 7.23	27.36 ± 9.19	0.995	...	0.31 ± 0.09	2.65
J090847.1+001512	6792	09^{m}08^{h}47^s.28	+00°15′14.″1	18.37 ± 18.37	18.16 ± 0.01	17.79 ± 0.01	17.45 ± 0.01	17.14 ± 0.01	17.55 ± 0.01	...	33.60 ± 6.38	6.58 ± 7.14	-1.24 ± 8.87	0.999	...	0.26 ± 0.05	2.71
J090324.0+003954	6893	09^{m}03^{h}23^s.95	+00°39′52.″1	21.76 ± 21.76	21.35 ± 0.11	20.98 ± 0.09	20.48 ± 0.13	19.86 ± 0.07	19.17 ± 0.01	19.32 ± 0.01	32.93 ± 6.49	16.27 ± 7.32	-0.91 ± 9.29	0.946	0.955	0.49 ± 0.19	2.54
J090808.2+002115	6962	09^{m}08^{h}08^s.14	+00°21′16.″5	22.38 ± 22.38	21.56 ± 0.13	21.07 ± 0.10	21.30 ± 0.27	20.14 ± 0.09	19.12 ± 0.01	...	32.57 ± 6.48	17.35 ± 7.23	-4.52 ± 9.05	0.997	...	...	1.28
J091308.7−005605	6991	09^{m}08^{h}08^s.80	−00°56′08.″0	>22.58	>21.33	>20.91	>19.72	>19.23	20.36 ± 0.03	20.03 ± 0.02	30.39 ± 6.44	38.53 ± 7.14	27.37 ± 8.94	0.987	0.986	...	2.47
J090915.4+003450	7107	09^{m}09^{h}15^s.06	+00°34′48.″8	20.68 ± 20.68	20.31 ± 0.04	19.99 ± 0.03	19.41 ± 0.04	19.00 ± 0.03	18.62 ± 0.01	18.81 ± 0.01	32.15 ± 6.41	8.28 ± 7.23	1.37 ± 9.01	0.972	0.976	0.74 ± 0.11	5.75
J090855.7+002121	7216	09^{m}08^{h}55^s.64	+00°21′23.″1	21.87 ± 21.87	21.44 ± 0.12	21.04 ± 0.09	20.82 ± 0.17	20.38 ± 0.11	19.34 ± 0.01	18.88 ± 0.01	32.34 ± 6.39	37.62 ± 7.16	33.56 ± 8.89	0.996	0.998	...	2.02
J090836.5+002513	7826	09^{m}08^{h}36^s.54	+00°25′09.″5	22.11 ± 22.11	21.54 ± 0.13	21.13 ± 0.10	21.16 ± 0.23	20.33 ± 0.11	19.41 ± 0.01	19.28 ± 0.01	30.94 ± 6.33	35.84 ± 7.13	27.94 ± 9.06	0.991	0.992	...	3.62
J090842.8+003623	8022	09^{m}08^{h}43^s.03	+00°36′21.″7	>21.85	>21.40	>20.94	>19.61	>19.20	20.96 ± 0.06	20.45 ± 0.03	29.66 ± 6.41	56.85 ± 7.21	50.43 ± 9.18	0.970	0.981	...	3.07
J091309.5−005417	9262	09^{m}08^{h}09^s.85	−00°54′19.″3	...	...	...	...	...	20.42 ± 0.02	20.04 ± 0.02	28.12 ± 6.57	39.70 ± 7.23	19.64 ± 9.22	0.958	0.954	...	4.46
J090830.0+002439	9290	09^{m}08^{h}29^s.79	+00°24′38.″1	>21.85	>21.40	>20.94	>19.61	>19.20	19.93 ± 0.02	19.72 ± 0.01	29.27 ± 6.47	38.29 ± 7.26	19.79 ± 8.98	0.754	0.770	...	3.45
J090909.4+003440	10110	09^{m}09^{h}09^s.80	+00°34′38.″5	>22.54	>21.73	>21.05	>19.74	>19.13	21.29 ± 0.05	20.62 ± 0.04	27.62 ± 6.52	37.27 ± 7.23	27.12 ± 9.02	0.558	0.861	...	5.06
J090820.3+002808	11918	09^{m}08^{h}19^s.84	+00°28′08.″6	22.34 ± 22.34	21.49 ± 0.13	21.16 ± 0.10	20.69 ± 0.15	20.53 ± 0.13	19.95 ± 0.03	19.99 ± 0.03	26.08 ± 6.45	37.76 ± 7.28	16.30 ± 9.11	0.764	0.787	...	6.92
J090834.7+003635	15947	09^{m}08^{h}34^s.77	+00°36′39.″1	...	...	...	...	...	20.55 ± 0.03	20.27 ± 0.02	22.52 ± 6.50	37.86 ± 7.14	32.28 ± 9.03	0.731	0.852	...	3.43

Notes. •ID with color–magnitude method.

[a] Coordinates are the position of IRAC counterparts.

[b] Photometry from the VIKING survey (Z, Y, J, H, K_s) is extracted in 2″ diameter apertures (W. Sutherland et al., in preparation).

[c] The reported SPIRE 350 and 500 μm fluxes are measured at the positions of 250 μm sources; no S/N cut is applied.

[d] R is reliability of the counterparts calculated separately at 3.6 and 4.5 μm from the LR method (Section 3.1).

[e] Redshifts are from the SDSS catalog for sources detected in that survey.

[f] The separation between the centroid of the SPIRE emission and the IRAC counterpart.

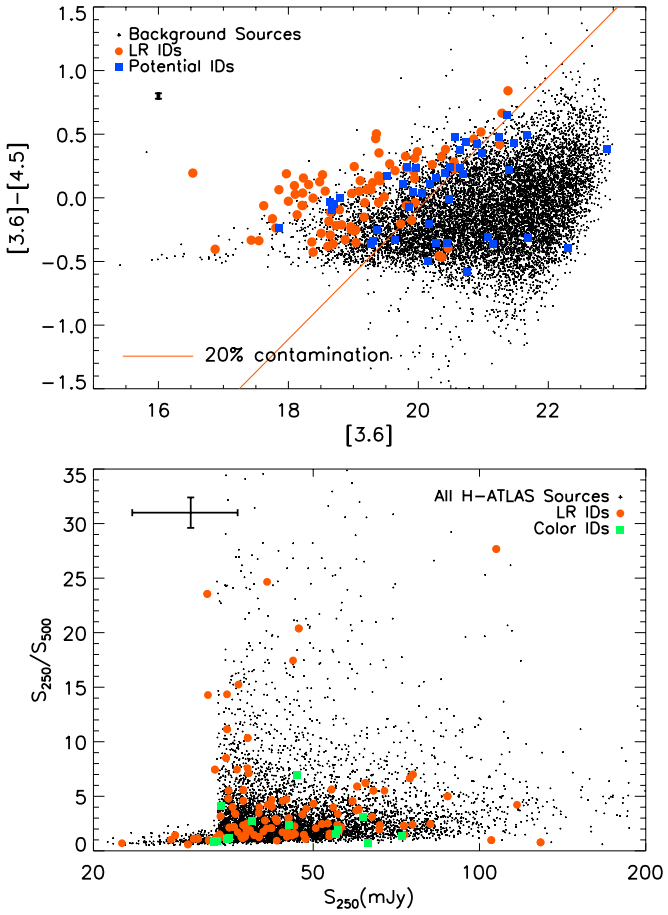

Figure 4. Top: IRAC color–magnitude diagram. All LR counterparts with $R \geqslant 0.8$ and potential counterparts are highlighted. Potential counterparts are IRAC galaxies within 7.″2 of SPIRE sources that are not otherwise identified with the LR method. The LR counterparts typically have $[3.6] - [4.5] > -0.4$ and are brighter than the background IRAC population. IRAC galaxies above the solid line and within 7.″2 of SPIRE positions have a probability of $\leqslant$20% of being random associations. This discriminator is used to identify an additional 23 IRAC counterparts to 13 SPIRE sources ("color IDs"; Section 3.4). Bottom: SPIRE color–flux diagram for all sources in the H-ATLAS SDP field. We highlight sources with identified IRAC counterparts using the LR and color–magnitude methods. Sources that have formal 500 μm fluxes below the 1σ detection limit are shown as lower limits and are excluded from the statistical analysis. A two-dimensional K-S test between the background population and the identified SPIRE sources yields the probability that the two data sets are drawn from the same parent population of $p = 0.172$. Thus, we conclude that the identified galaxies are not a strongly biased subsample of SPIRE sources, although there may be a small selection effect. Average error bars are shown at the top-left-hand corner of both plots.

(A color version of this figure is available in the online journal.)

by summing the probabilities of finding a background galaxy within 7.″2 of a SPIRE source occupying a distinct region of color–magnitude space.

In Figure 4, we show the S_{250}/S_{500} color–flux plot for H-ATLAS SDP sources and consider whether sources with identified IRAC counterparts are representative of the whole SPIRE population. A two-dimensional Kolmogorov–Smirnov (K-S) test between the background H-ATLAS SPIRE population and the sources with identified counterparts has $p = 0.172$, suggesting that the two samples are drawn from similar, but not necessarily identical, parent populations. Considering the S_{250}/S_{500} color and 250 μm fluxes separately yields $p = 0.710$ and $p = 0.289$, respectively. Thus, we conclude that the sources with identified IRAC counterparts are very similar to the whole

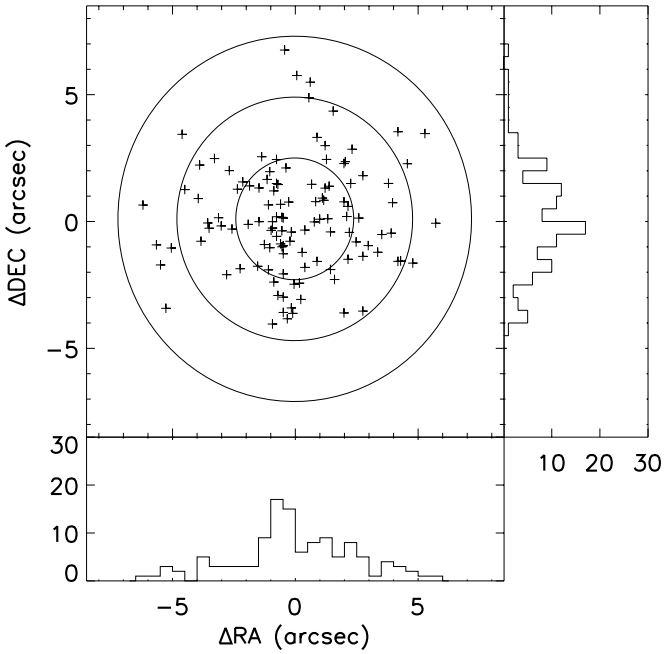

Figure 5. Distribution of ΔR.A. and Δdecl. offsets between SPIRE sources and the corresponding IRAC counterparts identified in this work. The astrometric median separation between SPIRE sources and IRAC is 0.″10 which is consistent with the overall IRAC astrometric uncertainty tied to the SDSS astrometry. The three concentric circles have radii of 1, 2, and $3\sigma_{\rm pos}$ (7.″2) from the SPIRE centroid. The overall offsets in R.A. and decl. show that there is no systematic offset between input SPIRE and IRAC sources.

SPIRE population, but may have a slightly different distribution of 250 μm flux.

3.5. Astrometric Offset

To check whether there is any noticeable astrometric shift among the input catalogs for LR analysis, in Figure 5 we plot the positional differences between the SPIRE sources and the corresponding IRAC counterparts. The median separation between SPIRE and IRAC sources is 0.″10. We also investigate the overall astrometric reference frame difference between IRAC and SDSS catalogs, using ~40% of the IRAC sample that is also identified with SDSS galaxies within 2″. The positional difference between IRAC and SDSS is $0.''19 \pm 0.''17$ and we found no systematic offset either in R.A. or decl.

Our IRAC data are complemented with VIKING Z, Y, J, H, and K_s-band photometry, which is measured in 2″ diameter apertures (W. Sutherland et al., in preparation). We cross-match the IRAC (FWHM ~ 1.″6) to the nearest-neighbor VIKING (FWHM ~ 0.″9) source within a 2″ search radius. Indeed, the mean offset between the IRAC and VIKING positions is $0.''09 \pm 0.''50$ and $0.''28 \pm 0.''28$ in R.A. and decl., respectively. We find no statistically significant astrometric error between the two catalogs.

4. DISCUSSION

As described in Sections 3.3 and 3.4, we identified IRAC counterparts to 136 (86%) of the SPIRE sources. Of these, 123 are identified with the LR method, and 23 counterparts to 13 SPIRE sources are identified with the color–magnitude method (Table 1). The contamination rate of 1.9% for the LR method is smaller than that from the color–magnitude method (12.6%) but corresponds to a similar number of IRAC galaxies—two

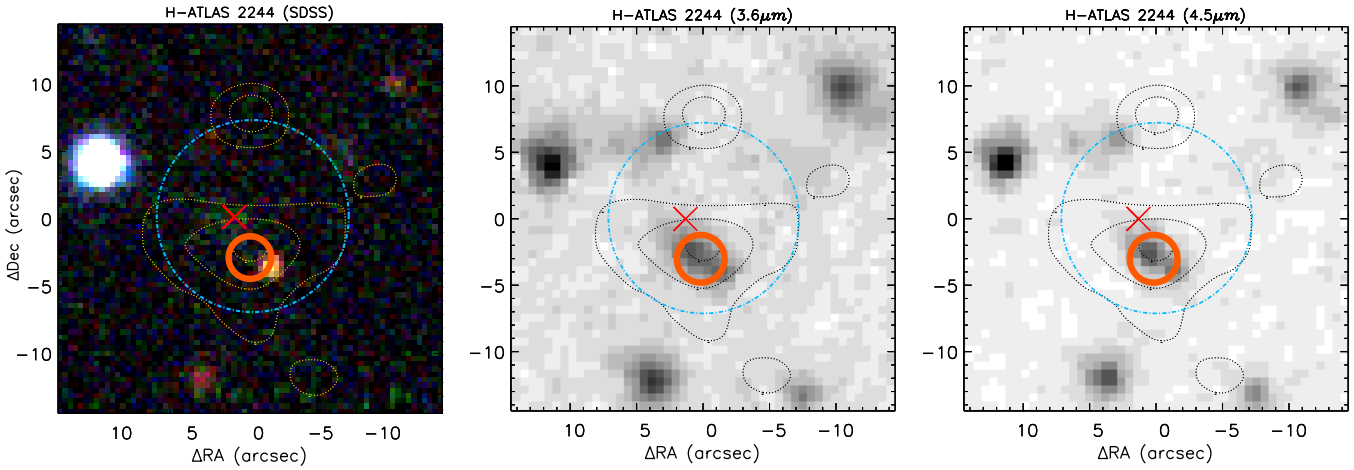

Figure 6. H-ATLAS ID-2244: an example of the source that is identified using the LR method, but where the IRAC counterpart ($R = 0.99$ at both 3.6 and 4.5 μm) is different from the SDSS counterpart (SDP.2244, $R = 0.97$; Smith et al. 2011). From left to right we show a three-color SDSS image (g, r, and i bands), the 3.6 μm, and the 4.5 μm data. The galaxies identified as the SDSS (SDP.2244) and IRAC (H-ATLAS ID-2244) counterparts to the SPIRE source are marked with an "X" and a small circle, respectively. The large circle has 7.″2 radius and encompasses the SPIRE $3\sigma_{\rm pos}$ area in which counterparts are identified. Contours show the SPIRE 250 μm emission at 5σ, 7σ, 9σ, 11σ levels. In the absence of high-resolution sub-mm imaging, we cannot determine whether this SPIRE source is the result of blended emission from the two identified galaxies, or whether one of those counterparts is a chance association.

(A color version of this figure is available in the online journal.)

to three. Combining the results from the two identification methods, we expect that the total false identification rate of the catalog presented in Table 2 is 3.6%, such that five to six of the IRAC counterparts presented in Table 2 are false.

4.1. Statistics of Identified Sources

We next compare the counterparts identified in the IRAC data with results based on SDSS (Smith et al. 2011). Of the 146 IRAC counterparts, 102 (70%) are undetected in SDSS, 52 (36%) agree with the SDSS identification, and two (1%) are different galaxies to the SDSS counterparts. On the basis of the false-identification rates of the two studies (4.2% for SDSS and 3.6% for IRAC) approximately four counterparts are expected to disagree between the two surveys, which is consistent with that observed here.

The two sources with different counterparts identified in IRAC and SDSS are H-ATLAS ID-2244 and 6962. We show one of these sources, H-ATLAS ID-2244, as an example in Figure 6. In this case, the SDSS (SDP.2244) and IRAC (H-ATLAS ID-2244) counterparts are separated by 3.″2 and both have a $\leqslant 3\%$ probability of being false identifications: $R = 0.97$ in SDSS and $R = 0.99$ at both 3.6 and 4.5 μm. In the absence of additional data, such as sub-mm or radio interferometry, the true nature of this source is unclear. It is possible that one of the counterparts is a chance association, although we cannot say which one. It is also possible that the SPIRE source is comprised of a blend of emission from both counterparts in a single SPIRE beam.

Blending is also an important consideration for counterparts that are identified with the color–magnitude method. Of the 13 SPIRE sources, 7 identified with this method have multiple IRAC counterparts; conversely the LR method has none. This apparent disparity is not surprising because the LR method implicitly assumes that each SPIRE source has a single IRAC counterpart. Where there are N multiple counterparts contributing equally to the sub-mm flux, the average R cannot exceed $1/N$, and will typically be $\sim 1/N$. Due to the large SPIRE beam (FWHM = 18.″1 at 250 μm), it is likely that in at least a few cases a single SPIRE source may be composed of blended emission from multiple galaxies or from galaxy interactions. The color–magnitude method does not consider the presence of other IRAC sources and is therefore not biased against multiple counterparts. In addition, beyond requiring that counterpart lie within the SPIRE counterpart search radius, the color–magnitude method does not consider the separation between the SPIRE and IRAC centroids and therefore it is not biased against wide-separation counterparts. However, it does require both 3.6 and 4.5 μm fluxes and it assumes that all SPIRE sources have a similar color–magnitude distribution at 3.6 and 4.5 μm.

The seven SPIRE sources in the sample that have multiple IRAC counterparts are likely to be a combination of blended SPIRE sources and individual sub-mm galaxies associated with multiple interacting IRAC sources. H-ATLAS ID-891 is shown as an example in Figure 7. In this case all the detected SDSS galaxies are $\gtrsim$3.″5 away from the SPIRE centroid and all have $R < 0.8$ (Smith et al. 2011). There are two potential counterparts in the IRAC data that are not detected in SDSS. Using the LR method alone, these two nearby sources have reliability of $R =$ 0.41 and 0.44 at 3.6 μm and $R = 0.47$ and 0.50 at 4.5 μm. However, both galaxies have [3.6] and [4.5] that place them in the region of color–magnitude space with <20% probability of being random associations with the SPIRE emission and as such they are both identified as counterparts. The two galaxies have similar colors, with $([3.6] - [4.5]) = 0.38$ and 0.43 mag, consistent with a redshift of $z \gtrsim 1.4$ (Papovich 2008). The two IRAC sources are separated by 2.″9 (24.9 kpc at $z = 2$, 23.0 kpc at $z = 3$). Furthermore, the SPIRE source is bright ($S_{500} = 84 \pm$ 9 mJy) and red in the sub-mm bands, with a rising spectrum from 250 to 500 μm, indicating a sub-mm photometric redshift of $z \gtrsim 3$ (e.g., Lapi et al. 2011), although we caution that the dust temperature and redshift are degenerate in the sub-mm bands. It is likely that H-ATLAS ID-891 is a blend of emission from the two identified counterparts and it is possible that the sub-mm emission is the result of a merger or interaction of two gas-rich galaxies (e.g., Aravena et al. 2010b). Spectroscopic data are required to verify this scenario, and we identify ID-891 as a target for additional follow-up, especially to identify the exact nature of the sub-mm emission.

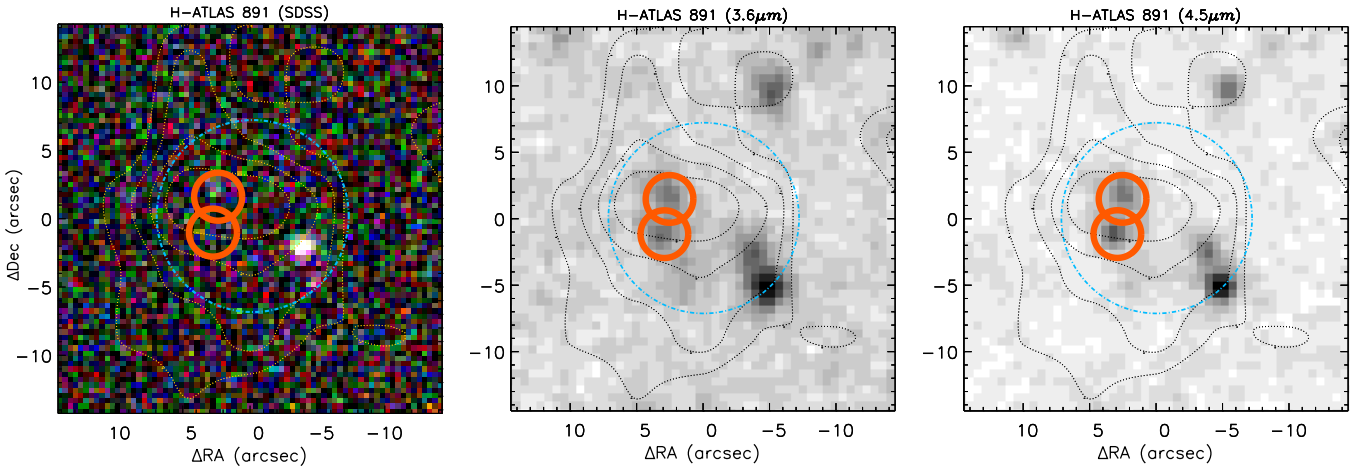

Figure 7. H-ATLAS ID-891: an example of counterpart identification using the color–magnitude method. Symbols are as in Figure 6. There is no LR counterpart in the SDSS r band (Smith et al. 2011) or with IRAC at 3.6 or 4.5 μm. However, there are two galaxies that are both identified as SPIRE counterparts on the basis of their IRAC colors and magnitudes. These two galaxies have $R = 0.41$ and 0.47 at 3.6 μm, and $R = 0.44$ and 0.50 at 4.5 μm, and neither is detected in SDSS. It is probable that the SPIRE source is a blend of the emission from these two IRAC galaxies although, in the absence of spectroscopic redshifts, it is unclear whether the configuration is caused by a line-of-sight alignment or an interaction between the two IRAC galaxies.

(A color version of this figure is available in the online journal.)

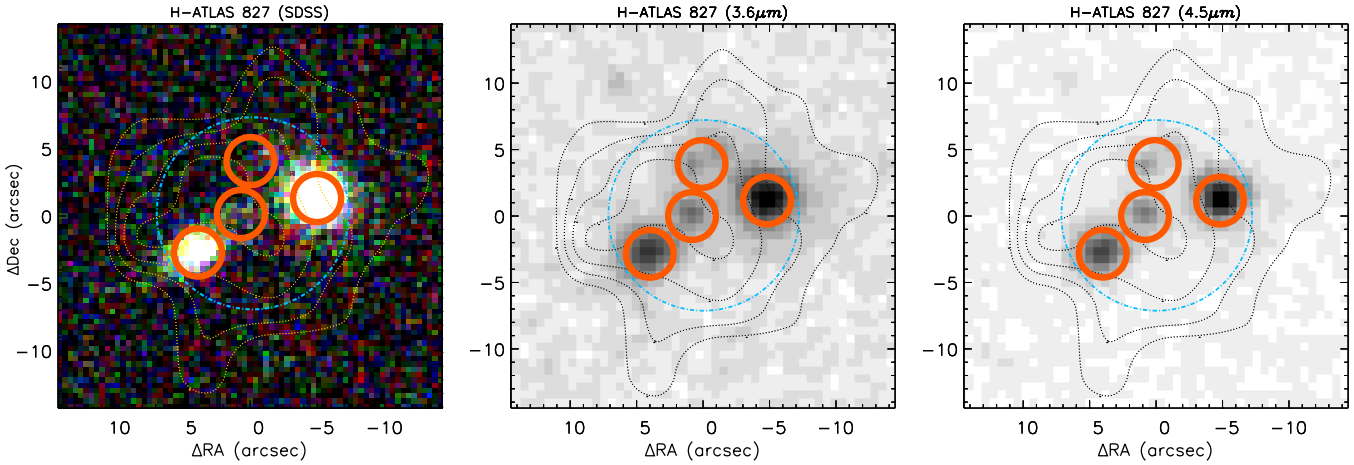

Figure 8. H-ATLAS ID-827 has four counterparts identified with the IRAC color–magnitude method and is the most complex system in our sample. The westernmost and easternmost galaxies are detected by SDSS (but are not identified as counterparts in these data; Smith et al. 2011), and have photometric redshifts of $z = 0.07 \pm 0.01$ and $z = 0.20 \pm 0.03$, respectively. The two fainter counterparts are not detected in SDSS but have $[3.6] - [4.5] > 0$, indicating that they may be at $z \gtrsim 1.4$ (Papovich 2008). We conclude that the SPIRE source is most likely to be comprised of blended emission from the four galaxies. Symbols are as in Figure 6.

(A color version of this figure is available in the online journal.)

H-ATLAS ID-827, shown in Figure 8, is the most complex system in our sample. In this case there are four IRAC counterparts identified on the basis of their colors and magnitudes. The four galaxies have a wide range of [3.6] with values from 17.8 mag to 20.2 mag. The counterparts do not appear to be clustered, as may be expected for gravitational lensing or a multi-component interaction, and each is separated from its nearest neighbor by $\sim 4''$. The two brightest galaxies are detected by SDSS, but were not identified as SPIRE counterparts by Smith et al. (2011); they have photometric redshifts of $z = 0.07 \pm 0.01$ and $z = 0.20 \pm 0.03$ for the westernmost and easternmost, respectively. The two fainter counterparts are not detected in SDSS and both have $[3.6] - [4.5] > 0$, indicating that they are likely to be at $z \gtrsim 1.4$ (Papovich 2008). The morphology, astrometry, and available redshift information suggest that gravitational lensing in unlikely and that H-ATLAS ID-827 is most likely to be a blended source, which is comprised of two low-redshift and two high-redshift components.

4.2. Redshifts of Identified Sources

Knowledge of the redshift distribution of SPIRE sources is central to understanding their role in the universe. However, only 50% of the IRAC counterparts are detected in SDSS and 74% have VIKING photometry. Therefore, any redshift distribution derived from the optical data will be biased to low redshifts where the detection rates in these surveys are high. Instead, in Figure 9 we plot the $[3.6] - [4.5]$ color distribution, and $[3.6] - [4.5]$ against redshift for the counterparts with spectroscopic or photometric redshift from SDSS. This plot includes the 104 IRAC counterparts that have both 3.6 and 4.5 μm coverage, 47 of which have an optical redshift. All of the optical redshift are $z < 0.8$; 32 (68%) of these galaxies have $([3.6]-[4.5]) < 0$, while 15 (32%) have $([3.6]-[4.5]) > 0$. The 57 identifications without reliable redshifts from the optical are undetected in SDSS and 43 of them have $([3.6] - [4.5]) > 0$, a crude indicator that $z \gtrsim 1.4$ (e.g., Papovich 2008). Thus, up to $\sim$40% of the identified SPIRE population may lie at

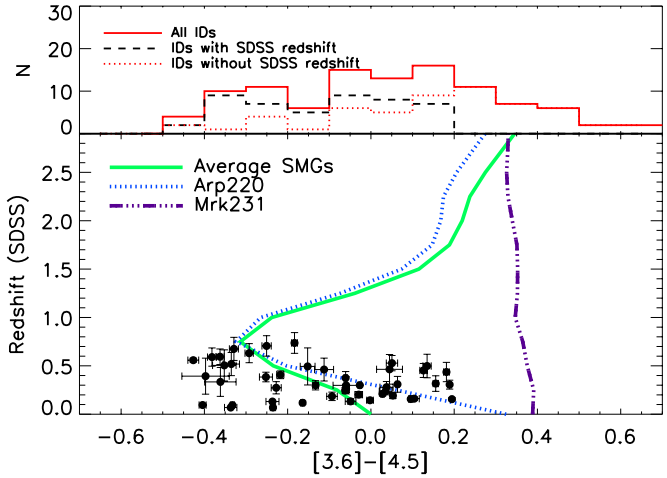

Figure 9. Distribution of IRAC [3.6] − [4.5] color for SPIRE counterparts with photometry at both wavelengths. For the 47 sources with SDSS spectroscopic or photometric redshifts, we also plot the [3.6] − [4.5] color against redshift. The 57 SPIRE-IRAC identifications without reliable redshifts are either faint or undetected in SDSS and 43 of them have [3.6] − [4.5] > 0, an indicator of high-redshift source ($z \gtrsim 1.4$; Papovich 2008). We expect that more than half of the sub-mm bright sources reside at $z \gtrsim 1.4$. For reference, the color–redshift tracks of Arp 220 (Silva et al. 1998), Mrk231 (Berta 2006), and the average sub-mm galaxy SED (Wardlow et al. 2011) are shown.

(A color version of this figure is available in the online journal.)

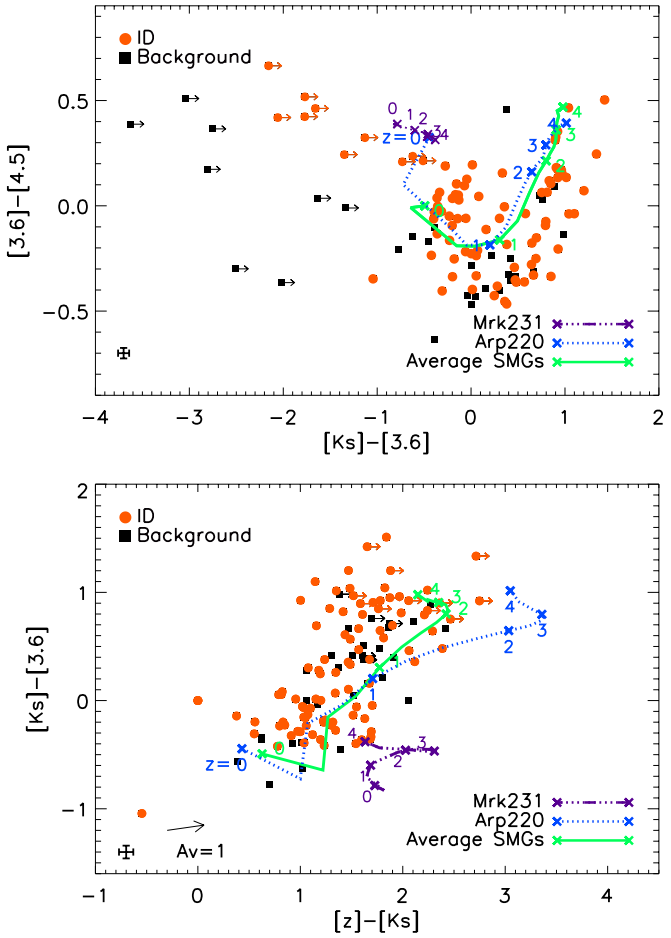

Figure 10. IRAC and VIKING color–color diagrams. Top: [K_s], [3.6], and [4.5]. Bottom: [z'], [K_s], and [3.6]. We highlight SPIRE counterparts and background sources that are within 7.″2 of SPIRE centroids. Tracks for Arp 220 (Silva et al. 1998), Mrk 231 (Berta 2006), and the average 870 μm selected sub-mm galaxies (Wardlow et al. 2011) are shown, and an $A_V = 1$ mag reddening vector and the median error bar are plotted in the lower left-hand corner. The SPIRE counterparts are slightly bluer than both these tracks, suggesting that they may have less dust reddening and A_V values that are 0.5–1 mag smaller than the SED templates.

(A color version of this figure is available in the online journal.)

high redshifts. Deep spectroscopy and photometry, particularly at near-IR wavelengths, is required to determine more precise redshift information.

We also investigate the redshift distribution of the SPIRE sources by calculating sub-mm photometric redshifts from the fluxes of the three SPIRE bands. We employ a template fitting method which uses χ^2 minimization, comparing the observed fluxes to the SEDs of Arp 220 (Silva et al. 1998) and Mrk 231 (Berta 2006). We caution that the sub-mm photometric redshifts are limited by the absence of longer wavelength data, and the degeneracy between redshift and dust temperature. Furthermore, flux boosting is an important consideration and will add significant errors to the fluxes of the faintest sources. Due to these uncertainties, we do not consider the sub-mm photometric redshifts on a source-by-source basis, but instead examine the overall distribution.

This sub-mm photometric redshift distribution peaks at $z \sim 2$ with a tail out to $z \sim 4$, and suggests that the majority of the IRAC counterparts without SDSS redshifts lie at $z \sim 2$. This result is consistent with the photometric redshifts of the whole SPIRE population (e.g., Amblard et al. 2010; Lapi et al. 2011) and the redshift distribution of 850 μm sources (e.g., Chapman et al. 2005; Wardlow et al. 2011). Now that the counterparts to a significant majority of SPIRE sources are known, follow-up spectroscopic campaigns to establish the redshifts of all the sources are feasible.

4.3. Properties of Identified Sources

Near-IR colors. In Figure 10 we show IRAC and VIKING color–color diagrams, highlighting identified SPIRE counterparts in comparison with background sources that are within 7.″2 of the SPIRE centroids. As we show in Figure 4 the SPIRE counterparts have distinct [3.6] − [4.5] color compared to the background sources, but the two populations are indistinguishable in [K_s] − [3.6] and [z] − [K_s]. We also compare to the redshift tracks of Arp 220 (Silva et al. 1998), Mrk 231 (Berta 2006), and the average 870 μm selected sub-mm galaxy (Wardlow et al. 2011). The SPIRE counterparts are slightly bluer than both these tracks suggesting that they may have less dust reddening and A_V values that are 0.5–1 mag smaller than the SED templates.

IR luminosities and dust temperatures. To understand properties of the identified H-ATLAS/IRAC galaxies associated with SDSS redshifts, we first consider an SED analysis of the SPIRE data making use of the redshifts based on the IRAC identification. First, we consider the far-IR/sub-mm portion of the SED with three-band SPIRE fluxes at 250, 350, and 500 μm and reproduce the analysis of Amblard et al. (2010) where the dust temperature (T_d) and IR luminosities L_{IR} were studied. We make use of a modified blackbody with isothermal dust temperature to describe the dust emission, in which flux can be written as

$$f_\mu \propto \mu^{3+\beta} e^{(h\mu/kT_d - 1)}. \quad (9)$$

To be consistent with previous other estimates from the literature, we fix $\beta = 1.5$ and fit to the SPIRE fluxes to establish the dust temperature and the overall normalization to the SED. The IR luminosity is estimated from the best-fit SED over the

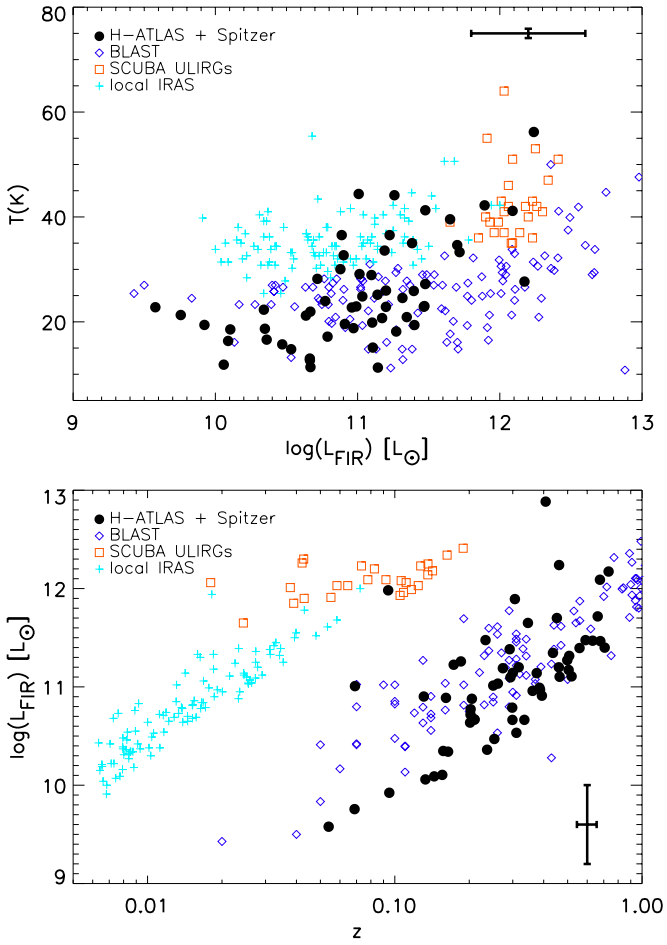

Figure 11. Top: dust temperature as a function of the infrared luminosity $L_{\rm IR}$ (8–1100 μm) for H-ATLAS/IRAC galaxies with SDSS redshifts. $L_{\rm IR}$ is obtained by fitting the SPIRE flux with $\beta = 1.5$ in isothermal modified blackbody model (Equation (9)). Error bars are median 1σ standard deviation from the best-fit models with dust temperature ($T_{\rm d}$) and total IR luminosities $L_{\rm IR}$ as free parameters. Bottom: dust temperature as a function of the redshift for H-ATLAS/IRAC galaxies. See the text for the comparison galaxy samples plotted here.

(A color version of this figure is available in the online journal.)

wavelength range of 8–1100 μm. Since we only fit to the dust emission at wavelengths greater than 250 μm, our luminosities are likely low by a factor of 2–3 if there is any warm dust, heated by active galactic nuclei, present in these galaxies. However, our overall uncertainty on the IR luminosity estimates is at least a factor of five. For the sample as a whole we find an average dust temperature of 26 ± 9 K, which compares well with the average dust temperature of 27 ± 8 K for $z < 0.1$ SPIRE galaxies based on SDSS identifications only (Amblard et al. 2010).

We summarize our results related to the FIR SED analysis in Figure 11 where we show the $L_{\rm IR}$–$T_{\rm d}$ relation and the $L_{\rm IR}$ as a function of the redshift, determined from the reliable H-ATLAS IDs with either SDSS spectroscopic or photometric redshift. We also compare the H-ATLAS dust temperatures and IR luminosities with sub-mm bright galaxy samples in the literature. Samples include the sources in BLAST with COMBO-17 (Wolf et al. 2004) or a SWIRE photometric redshift (Rowan-Robinson et al. 2008) and *Spitzer*-MIPS 70 and 160 μm fluxes (Dye et al. 2009), local ULIRGs observed with SCUBA at 450 and 850 μm (Clements et al. 2010), and local *IRAS*-selected galaxies with 60 and 100 μm fluxes along with SCUBA 850 μm (Dunne et al. 2000).

In Figure 11, we find that the SPIRE-selected galaxies in H-ATLAS with IRAC-based identifications for redshifts span the luminosity range of 10^{10}–10^{12} $L_{\odot}$ from sub-LIRG luminosities to ULIRG conditions. These luminosities and the ranges are comparable to BLAST-detected sources, while they span lower than the local *IRAS*-selected galaxies, which tend to be at lower redshifts $z < 0.05$ and have higher luminosities; such a difference is understandable since *IRAS* is an all-sky shallow survey and detects primarily the rare, bright galaxies in the nearby universe.

Stellar masses and star formation rates. With the cross-identification we can expand the SED analysis over three orders of magnitude in wavelength from optical to sub-mm. For optical and near-IR data we make use of SDSS, UKIDSS (Lawrence et al. 2007), VIKING (W. Sutherland et al., in preparation), and IRAC 3.6 and 4.5 μm fluxes. The analysis of full optical to sub-mm SEDs is similar in spirit to Dunne et al. (2011) where the SEDs of SPIRE sources with reliable identifications using SDSS data were analyzed. We make use of the MAGPHYS SED modeling code (da Cunha et al. 2008) for this work. The SED modeling in the code is done in an energy-balance manner such that the absorbed light in shorter UV and optical wavelengths is accounted for by the thermal re-radiation at far-infrared and sub-mm wavelengths. For the H-ATLAS/IRAC galaxy sample we have five optical fluxes from SDSS (u, g, r, i, z), five near-IR fluxes from UKIDSS+VIKING ($Z, Y, J, H, K_{\rm s}$), and two IRAC channels (3.6, 4.5 μm), in addition to three SPIRE bands. Redshift information of the sources are from SDSS spectroscopic observations ($z = 0$–0.8).

For comparative work with other sub-mm galaxy samples, we focus on results related to stellar mass $M_{\star}$ and star formation rate (SFR), as given by MAGPHYS best-fit models. In Figure 12 (top figure), we plot the specific star formation rate (sSFR) given as SFR/$M_{\star}$ versus redshift with our sample sub-divided to two stellar mass bins. We find that the sSFR of IRAC IDs marginally show an anticorrelation with galaxy stellar mass. Such a behavior may be related to the *downsizing* scenario (Cowie et al. 1996).

However, when compared to Damen et al. (2009) and Pérez-González et al. (2008), IRAC IDs show 0.4 $\sim$ 0.5 dex higher sSFRs. The Damen et al. (2009) galaxy sample is an IRAC-selected sample of galaxies out to $z \sim 1.8$ in ECDFS with photometry supplemented with optical, near-IR, and MIPS 24 μm fluxes. The Pérez-González et al. (2008) sample is selected with IRAC at 3.6 and 4.5 μm in a variety of fields. While our SPIRE-selected sample has IRAC identifications, they are not likely to be the majority of the galaxies in both these studies. This is also clear from Figure 4 where we show that most of the identified SPIRE sources are distributed differently from the background population in the color–magnitude space. They occupy the top end of the star formation in galaxies selected at near-IR wavelengths.

In Figure 12 (bottom), we plot the SFR versus the stellar mass of our sample. The SFR of *normal* local star-forming galaxies at $z \sim 1$ is known to correlate strongly with the stellar mass and form the so-called *star formation main sequence* (Brinchmann et al. 2004; Salim et al. 2007; Peng et al. 2010). Such a correlation is also observed at higher redshifts, albeit with a different normalization (e.g., Daddi et al. 2007, 2009; Elbaz et al. 2007; Noeske et al. 2007; Pannella et al. 2009; González et al. 2010; Rodighiero et al. 2010; Karim et al. 2011).

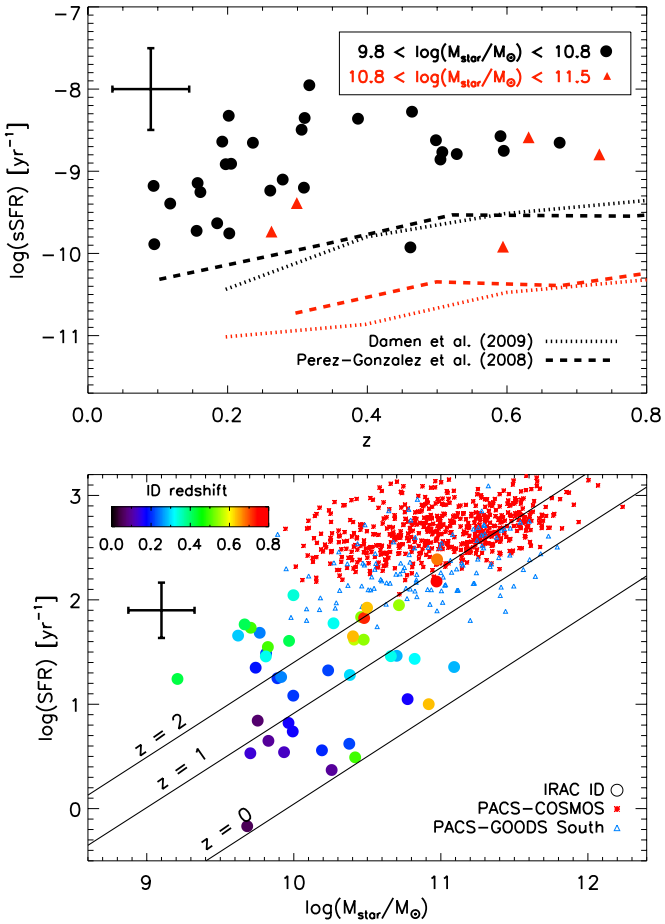

Figure 12. Top: specific star formation rate (sSFR) for our IRAC-identified SPIRE galaxies as a function of the redshift. Filled circles and triangles represent H-ATLAS galaxies in stellar mass bins $10^{9.8}$–$10^{10.8}$ $M_{\odot}$ and $10^{10.8}$–$10^{11.5}$ $M_{\odot}$, respectively. Our data are compared to Pérez-González et al. (2008) and Damen et al. (2009). Upper (lower) two lines are for the smaller (larger) mass bin. The error bar on the top left shows the average 68% confidence range on log(sSFR). Bottom: star formation rate as a function of the stellar mass. We plot results from a previous study for comparison: PACS-COSMOS and PACS-GOODS South (Rodighiero et al. 2011). We also show the mean SFR and stellar mass correlation at $z = 2$ (Daddi et al. 2007), 1, and 0 (Elbaz et al. 2007). The majority of the H-ATLAS/IRAC galaxies fall between $z = 0 \sim 2$ in the SFR–$M_{\star}$ relation showing a slight excess of star formation rate compared with populations at similar redshifts, but selected at optical and near-IR wavelengths.

(A color version of this figure is available in the online journal.)

However, the typical dispersion of correlation is known to be $\sim$0.3 dex over a wide range of redshifts $z = 0 \sim 2$.

Local (U)LIRGs and high-redshift submillimeter galaxies (SMGs) have SFRs in excess of the main sequence and are defined as starburst galaxies (e.g., Elbaz et al. 2007, 2011). These galaxies generally occupy a region that is $\sim\times 10$ above the main sequence. However, there is also evidence that some high-redshift (U)LIRGs and SMGs do not have enhanced SFRs relative to their stellar mass and that the starburst fraction may decrease at high redshifts (e.g., Tacconi et al. 2008; Rodighiero et al. 2011). This suggests changes to the mode of star formation in (U)LIRGs between $z = 0$ and $z = 2$ away from the starburst mechanism (e.g., Genzel et al. 2010; Daddi et al. 2010; Elbaz et al. 2011; Krumholz et al. 2012; Melbourne et al. 2012). In our work, $\sim$50% of the subsample of IRAC-identified SPIRE galaxies ($z < 1$) lie near the starburst region. Thus, it is possible that half of the IRAC-identified SPIRE galaxies with SDSS redshifts are in fact starbursts that lie off the main sequence.

5. SUMMARY

We have identified *Spitzer*-IRAC counterparts to sources selected with *Herschel*-SPIRE at 250 μm in the H-ATLAS survey. Among 159 SPIRE centroids, we found 123 reliable IRAC counterparts using an LR analysis. The identified SPIRE sources are distributed differently in IRAC color–magnitude space compared to the field population. Therefore, we made an additional selection based on the IRAC ID locality to yield a further 23 counterparts to 13 SPIRE sources. Seven SPIRE sources have multiple IRAC counterparts. These are likely to be due to blended emission in the SPIRE beam.

In total, 146 reliable IRAC counterparts to 136 SPIRE sources were identified, including 7 that have more than 1 IRAC counterpart. The identification rate of 86% is higher than that of wide-field ground-based optical and near-IR imaging of *Herschel* fields. The galaxies with unknown redshifts and that are not detected in SDSS and VIKING imaging data have SPIRE colors indicative of high-redshift sources and $[3.6] - [4.5] > 0$, suggesting that they are likely to be at $z \gtrsim 1.4$. We estimate the $\sim$40% of SPIRE sources lie at high redshifts, although the exact redshift distribution of SPIRE sources remains elusive. The counterparts presented here can now be pursued for follow-up data to further investigate the nature of SPIRE galaxies. The majority of our detected galaxies with sub-LIRG to LIRG luminosities are not intense starbursting galaxies in the local universe, though they have above average sSFRs.

Herschel-ATLAS is a project which uses *Herschel*, an ESA space observatory with science instruments provided by European-led Principal Investigator consortia and with important participation from NASA. The H-ATLAS Web site is http://www.h-atlas.org/. This work is based in part on observations made with the *Spitzer Space Telescope*, which is operated by the Jet Propulsion Laboratory, California Institute of Technology, under a contract with NASA. Support for this work was provided by NASA through an award issued by JPL/Caltech. US participants in H-ATLAS also acknowledge support from the NASA Herschel Science Center through a contract from JPL/Caltech.

Funding for the SDSS and SDSS-II has been provided by the Alfred P. Sloan Foundation, the Participating Institutions, the National Science Foundation, the U.S. Department of Energy, the National Aeronautics and Space Administration, the Japanese Monbukagakusho, the Max Planck Society, and the Higher Education Funding Council for England. The SDSS Web site is http://www.sdss.org/.

The SDSS is managed by the Astrophysical Research Consortium for the Participating Institutions. The Participating Institutions are the American Museum of Natural History, Astrophysical Institute Potsdam, University of Basel, University of Cambridge, Case Western Reserve University, University of Chicago, Drexel University, Fermilab, the Institute for Advanced Study, the Japan Participation Group, Johns Hopkins University, the Joint Institute for Nuclear Astrophysics, the Kavli Institute for Particle Astrophysics and Cosmology, the Korean Scientist Group, the Chinese Academy of Sciences (LAMOST), Los Alamos National Laboratory, the Max-Planck-Institute for Astronomy (MPIA), the Max-Planck-Institute for Astrophysics (MPA), New Mexico State University, Ohio State University, University of Pittsburgh, University of Portsmouth, Princeton University, the United States Naval Observatory, and the University of Washington.

This work used data from VISTA at the ESO Paranal Observatory, program 179.A-2004. VISTA is an ESO near-infrared survey telescope in Chile, conceived and developed by a consortium of universities in the United Kingdom, led by Queen Mary University, London.

We thank Giulia Rodighiero for providing us electronic tables of COSMOS and GOODS SED fitting results. The UCI group acknowledges support from NSF CAREER AST-0645427, NASA NNX10AD42G, and an award from Caltech/JPL for US participation in *Herschel*-ATLAS.

REFERENCES

Abazajian, K. N., Adelman-McCarthy, J. K., Agüeros, M. A., et al. 2009, ApJS, 182, 543
Amblard, A., Cooray, A., Serra, P., et al. 2010, A&A, 518, L9
Aravena, M., Bertoldi, F., Carilli, C., et al. 2010a, ApJ, 708, L36
Aravena, M., Younger, J. D., Fazio, G. G., et al. 2010b, ApJ, 719, 15
Ashby, M. L. N., Stern, D., Brodwin, M., et al. 2009, ApJ, 701, 428
Austermann, J. E., Dunlop, J. S., Perera, T. A., et al. 2010, MNRAS, 401, 160
Barmby, P., Huang, J.-S., Ashby, M. L. N., et al. 2008, ApJS, 177, 431
Berta, S. 2006, PASP, 118, 754
Bertin, E., & Arnouts, S. 1996, A&AS, 117, 393
Biggs, A. D., Ivison, R. J., Ibar, E., et al. 2011, MNRAS, 413, 2314
Blain, A. W., Smail, I., Ivison, R. J., Kneib, J.-P., & Frayer, D. T. 2002, Phys. Rep., 369, 111
Bond, N., Benford, D. J., Gardner, J. P., et al. 2012, ApJ, 750, L18
Borys, C., Scott, D., Chapman, S., et al. 2004, MNRAS, 355, 485
Brand, K., Eisenhardt, P., Gorjian, V., Kochanek, C. S., et al. 2006, ApJ, 641, 140
Brinchmann, J., Charlot, S., White, S. D. M., et al. 2004, MNRAS, 351, 1151
Brusa, M., Zamorani, G., Comastri, A., et al. 2007, ApJS, 172, 353
Budavári, T., & Szalay, A. 2008, ApJ, 679, 301
Chapin, E., Pope, A., Scott, D., et al. 2009, MNRAS, 398, 1793
Chapman, S. C., Blain, A. W., Ivison, R. J., & Smail, I. 2003, Nature, 422, 695
Chapman, S. C., Blain, A. W., Smail, I., & Ivison, R. J. 2005, ApJ, 622, 772
Chen, C.-C., Cowie, L. L., Wang, W.-H., Barger, A. J., & Williams, J. P. 2011, ApJ, 733, 64
Ciliegi, P., Zamorani, G., Hasinger, G., et al. 2003, A&A, 398, 901
Clements, D. L., Dunne, L., & Eales, S. 2010, MNRAS, 403, 274
Clements, D. L., Vaccari, M., Babbedge, T., et al. 2008, MNRAS, 387, 247
Condon, J. J., Cotton, W. D., Greisen, E. W., et al. 1998, AJ, 115, 1693
Coppin, K., Chapin, E. L., Mortier, A. M. J., et al. 2006, MNRAS, 372, 1621
Cowie, L. L., Barger, A. J., Wang, W.-H., & Williams, J. P. 2009, ApJ, 697, L122
Cowie, L. L., Songaila, A., Hu, E. M., & Cohen, J. G. 1996, AJ, 112, 839
da Cunha, E., Charlot, S., & Elbaz, D. 2008, MNRAS, 388, 1595
Daddi, E., Dannerbauer, H., Stern, D., et al. 2009, ApJ, 694, 1517
Daddi, E., Dickinson, M., Morrison, G., et al. 2007, ApJ, 670, 156
Daddi, E., Elbaz, D., Walter, F., et al. 2010, ApJ, 714, 118
Damen, M., Labbé, I., Franx, M., et al. 2009, ApJ, 690, 937
Downes, A. J. B., Peacock, J. A., Savage, A., & Carrie, D. R. 1986, MNRAS, 218, 31
Downes, D., Neri, R., Greve, A., et al. 1999, A&A, 347, 809
Driver, S., Hill, D. T., Kelvin, L. S., et al. 2011, MNRAS, 413, 971
Dunlop, J. S., Ade, P. A. R., Bock, J. J., et al. 2010, MNRAS, 408, 2022
Dunne, L., Eales, S., Edmunds, M., et al. 2000, MNRAS, 315, 115
Dunne, L., Gomez, H. L., da Cunha, E., et al. 2011, MNRAS, 417, 1510
Dwek, E., Arendt, R. G., Hauser, M. G., et al. 1998, ApJ, 508, 106
Dye, S., Ade, P. A. R., Bock, J. J., et al. 2009, ApJ, 703, 285
Dye, S., Eales, S. A., Aretxaga, I., et al. 2008, MNRAS, 386, 1107
Eales, S., Dunne, L., Clements, D., et al. 2010, PASP, 122, 499
Eales, S., Lilly, S., Gear, W., et al. 1999, ApJ, 515, 518
Eisenhardt, P. R., Stern, D., Brodwin, M., et al. 2004, ApJS, 154, 48
Elbaz, D., Daddi, E., Le Borgne, D., et al. 2007, A&A, 468, 33
Elbaz, D., Dickinson, M., Hwang, H. S., et al. 2011, A&A, 533, 119
Fazio, G. G., Ashby, M. L. N., Barmby, P., et al. 2004a, ApJS, 154, 39
Fazio, G. G., Hora, J. L., Allen, L. E., et al. 2004b, ApJS, 154, 10
Fixsen, D. J., Dwek, E., Mather, J. C., Bennett, C. L., & Shafer, R. A. 1998, ApJ, 508, 123
Fleuren, S., Sutherland, W., Dunne, L., et al. 2012, MNRAS, 423, 2407
Garrett, M. A. 2002, A&A, 384, 19
Gear, W. K., Lilly, S. J., Stevens, J. A., et al. 2000, MNRAS, 316, 51
Genzel, R., Tacconi, L. J., Gracia-Carpio, J., et al. 2010, MNRAS, 407, 2091
González, V., Labbé, I., Bouwens, R. J., et al. 2010, ApJ, 713, 115
Gorjian, V., Brodwin, M., Kochanek, C. S., et al. 2008, ApJ, 679, 1040
Griffin, M. J., Abergel, A., Abreu, A., et al. 2010, A&A, 518, L3
Hatsukade, B., Iono, D., Akiyama, T., et al. 2010, ApJ, 711, 974
Hickox, R. C., Wardlow, J. L., Smail, I., et al. 2012, MNRAS, 421, 284
Hopwood, R., Wardlow, J., Cooray, A., et al. 2011, ApJ, 728, L4
Hughes, D. H., Serjeant, S., Dunlop, J., et al. 1998, Nature, 394, 241
Ibar, E., Ivison, R. J., Cava, A., et al. 2010, MNRAS, 409, 38
Iono, D., Peck, A. B., Pope, A., et al. 2006, ApJ, 640, L1
Ivison, R. J., Dunlop, J. S., Hughes, D. H., et al. 1998, ApJ, 494, 211
Ivison, R. J., Greve, T. R., Dunlop, J. S., et al. 2007, MNRAS, 380, 199
Ivison, R. J., Greve, T. R., Serjeant, S., et al. 2004, ApJS, 154, 124
Ivison, R. J., Greve, T. R., Smail, I., et al. 2002, MNRAS, 337, 1
Ivison, R. J., Morrison, G. E., Biggs, A. D., et al. 2008, MNRAS, 390, 1117
Karim, A., Schinnerer, E., Martínez-Sansigre, A., et al. 2011, ApJ, 730, 61
Krumholz, M., Dekel, A., & McKee, C. F. 2012, ApJ, 745, 69
Lapi, A., González-Nuevo, J., Fan, L., et al. 2011, ApJ, 742, 24
Lawrence, A., Warren, S. J., Almaini, O., et al. 2007, MNRAS, 379, 1599
Makovoz, D., & Marleau, F. R. 2005, PASP, 117, 1113
Matsuda, Y., Iono, D., Ohta, K., et al. 2007, ApJ, 667, 667
Melbourne, J., Soifer, B. T., Desai, V., et al. 2012, AJ, 143, 125
Negrello, M., Hopwood, R., De Zotti, G., et al. 2010, Science, 330, 800
Noeske, K. G., Weiner, B. J., Faber, S. M., et al. 2007, ApJ, 660, L43
Pannella, M., Gabasch, A., Goranova, Y., et al. 2009, ApJ, 701, 787
Papovich, C. 2008, ApJ, 676, 206
Pascale, E., Auld, R., Dariush, A., et al. 2011, MNRAS, 415, 911
Peng, Y.-J., Lilly, S. J., Kovač, K., et al. 2010, ApJ, 721, 193
Pérez-González, P. G., Rieke, G. H., Villar, V., et al. 2008, ApJ, 675, 234
Pilbratt, J., Riedinger, J. R., Passvogel, T., et al. 2010, A&A, 518, L1
Poglitsch, A., Waelkens, C., Geis, N., et al. 2010, A&A, 518, L2
Pope, A., Scott, D., Dickinson, M., et al. 2006, MNRAS, 370, 1185
Puget, J. L., Abergel, A., Bernard, J.-P., et al. 1996, A&A, 308, L5
Rigby, E. E., Maddox, S. J., Dunne, L., et al. 2011, MNRAS, 415, 2336
Rodighiero, G., Cimatti, A., Gruppioni, C., et al. 2010, A&A, 518, 25
Rodighiero, G., Daddi, E., Baronchelli, I., et al. 2011, ApJ, 739, L40
Rowan-Robinson, M., Babbedge, T., Oliver, S., et al. 2008, MNRAS, 386, 697
Salim, S., Rich, R. M., Charlot, S., et al. 2007, ApJS, 173, 267S
Schneider, D. P., Hall, P. B., Richards, G. T., et al. 2007, AJ, 134, 102
Scott, S. E., Fox, M. J., Dunlop, J. S., et al. 2002, MNRAS, 331, 817
Silva, L., Granato, G. L., Bressan, A., & Danese, L. 1998, ApJ, 509, 103
Smail, I., Ivison, R. J., & Blain, A. W. 1997, ApJ, 490, L5
Smith, D. J. B., Dunne, L., Maddox, S. J., et al. 2011, MNRAS, 416, 857
Smolčić, V., Aravena, M., Navarrete, F., et al. 2012a, A&A, accepted (arXiv:1205.6470)
Smolčić, V., Navarrete, F., Aravena, M., et al. 2012b, ApJS, 200, 10
Surace, J. A., Shupe, D. L., Fang, F., Lonsdale, C. J., Gonzalez-Solares, et al. 2005, http://swire.ipac.caltech.edu/swire/astronomers/publications
Sutherland, W., & Saunders, W. 1992, MNRAS, 259, 413
Tacconi, L. J., Genzel, R., Smail, I., et al. 2008, ApJ, 680, 246
Tamura, Y., Iono, D., Wilner, D. J., et al. 2010, ApJ, 724, 1270
Thompson, M., Smith, D. J. B., Stevens, J. A., et al. 2010, A&A, 518, L134
Wang, W.-H., Cowie, L. L., Barger, A. J., & Williams, J. P. 2011, ApJ, 726, L18
Wardlow, J. L., Smail, I., Coppin, K. E. K., et al. 2011, MNRAS, 415, 1479
Wolf, C., Meisenheimer, K., Kleinheinrich, M., et al. 2004, A&A, 421, 913
York, D. G., Adelman, J., Anderson, J. E., Jr., et al. 2000, AJ, 120, 1579
Younger, J. D., Dunlop, J. S., Peck, A. B., et al. 2008, MNRAS, 387, 707
Younger, J. D., Fazio, G. G., Huang, J.-S., et al. 2007, ApJ, 671, 1531
Younger, J. D., Fazio, G. G., Huang, J.-S., et al. 2009, ApJ, 704, 803